中国科学: 地球科学
SCIENTIA SINICA Terrae
earthcn.scichina.com
《中国科学》杂志社
SCIENCE CHINA PRESS
论 文

高灵敏度-单接收杯LA-SF-ICP-MS原位方解石U-Pb定年

吴石头[1,2], 杨岳衡[1,2*], Nick M. W. ROBERTS[3], 杨明[1,2], 王浩[1,2], 兰中伍[1,2], 谢博航[1,2], 李天义[4], 许蕾[1,2], 黄超[1,2], 谢烈文[1,2], 杨进辉[1,2], 吴福元[1,2]

1. 中国科学院地质与地球物理研究所岩石圈演化国家重点实验室, 北京 100029;
2. 中国科学院地球科学创新研究院, 北京 100029;
3. Geochronology and Tracers Facility, British Geological Survey, Environmental Science Centre, Nottingham NG12 5GG, UK;
4. 中国石油化工集团公司深部地质与资源重点实验室, 北京 102206
* 通讯作者, E-mail: yangyueheng@mail.iggcas.ac.cn

收稿日期: 2021-06-24; 收修改稿日期: 2022-01-24; 接受日期: 2022-02-18; 网络版发表日期: 2022-04-27
国家重点研发计划项目(编号: 2018YFA0702602)、国家自然科学基金项目(批准号: 41903024)和中国科学院青年创新促进会项目(编号: 2022066)资助

摘要 激光剥蚀电感耦合等离子体质谱(LA-ICP-MS)方解石U-Pb定年是一种新兴的地质年代学方法, 在解决一系列关键地质问题中具有广阔的应用前景. 由于方解石中U和Pb含量低, 采用高灵敏度扇形磁场电感耦合等离子体质谱仪(SF-ICP-MS)比四极杆电感耦合等离子体质谱仪(Q-ICP-MS)更有优势. 研究发现对于Thermo Element XR型号的SF-ICP-MS仪器, 当采用Jet+X锥组和N_2增敏技术时, U和Pb的灵敏度最佳. 提高灵敏度不仅能明显改善方解石定年分析精度, 而且可在高空间分辨率条件下(<110μm)实现低^{238}U(<1μg g^{-1})或^{207}Pb(如<10Ma)含量样品的定年测试. 对于NIST SRM 614、ARM-3和WC-1这三个标准物质来说, 在激光束斑85μm和能量密度~2.0J cm^{-2}的条件下, 由激光剥蚀产生的^{206}Pb/^{238}U动态分馏不显著(<2.2%). 在最佳仪器条件下, 系统分析了四个常用的方解石U-Pb标准物质(WC-1、Duff Brown Tank、JT和ASH-15). 结果与已发表的同位素稀释热电离质谱(ID-TIMS)数据相吻合, 验证了方法的可靠性. 研究进一步证明, 基于LA-ICP-MS二维元素成像技术辅助选取样品定年区域可提高方解石U-Pb定年的成功率.

关键词 方解石U-Pb年代学, SF-ICP-MS, LA-ICP-MS, 高灵敏度, Jet采样锥

1 引言

方解石作为原生和次生矿物, 可以在多种地质环境中形成, 包括成岩过程、生物作用、岩浆、变质和热液过程(Roberts等, 2020). 方解石形成过程中, 微量的铀(U)可以进入方解石, 使其成为一种潜在的U-Pb定年对象(Moorbath等, 1987; Smith等, 1991; Jahn和Cuvellier, 1994; Woodhead等, 2006). 方解石U-Pb年代学

中文引用格式: 吴石头, 杨岳衡, Roberts N M W, 杨明, 王浩, 兰中伍, 谢博航, 李天义, 许蕾, 黄超, 谢烈文, 杨进辉, 吴福元. 2022. 高灵敏度-单接收杯LA-SF-ICP-MS原位方解石U-Pb定年. 中国科学: 地球科学, 52, doi: 10.1360/N072021-0165
英文引用格式: Wu S, Yang Y, Roberts N M W, Yang M, Wang H, Lan Z, Xie B, Li T, Xu L, Huang C, Xie L, Yang J, Wu F. 2022. *In situ* calcite U-Pb geochronology by high-sensitivity single-collector LA-SF-ICP-MS. Science China Earth Sciences, 65, https://doi.org/10.1007/s11430-021-9907-1

在诸多地学领域具有较大的应用前景, 如古气候(Woodhead等, 2006, 2012; Woodhead和Petrus, 2019; Kurumada等, 2020)、沉积学(Drost等, 2018; Montano等, 2021)、成岩作用(Smith等, 1991)、断裂时代(Roberts和Walker, 2016; Goodfellow等, 2017; Nuriel等, 2017; Hansman等, 2018; Parrish等, 2018; Yang等, 2021)、成矿过程(Burisch等, 2017; Shen等, 2019; Pan等, 2020)以及油气运移(Holdsworth等, 2019; Rochelle-Bates等, 2021)等. 早期方解石U-Pb定年主要基于同位素稀释法(ID), 然后采用热电离质谱(TIMS)或多接收电感耦合等离子体质谱(MC-ICP-MS)进行测定(Moorbath等, 1987; Smith等, 1991; Jahn和Cuvellier, 1994; Woodhead等, 2006). 然而, 这种分析方法耗时长, 需要样品溶解以及U和Pb的化学分离; 其空间分辨率差, 不适合用于具有环带变化的样品, 因此并没有得到广泛应用.

自激光剥蚀电感耦合等离子体质谱(LA-ICP-MS)首次应用于化石中方解石胶结物U-Pb定年以来(Li等, 2014), 该技术已在多个实验室得到了推广和应用(Coogan等, 2016; Ring和Gerdes, 2016; Goodfellow等, 2017; Drost等, 2018; Pagel等, 2018; Parrish等, 2018; Yokoyama等, 2018; Woodhead和Petrus, 2019; Cheng等, 2020; Guillong等, 2020; Kurumada等, 2020; Luo等, 2020; Pan等, 2020; Hoareau等, 2021; Yang等, 2021). 与ID-TIMS/MC-ICP-MS相比, LA-ICP-MS具有空间分辨率高、分析速度快等优点, 能快速得到U-Pb比值显著变化的大量数据. 然而, 方解石U含量普遍较低, Roberts等(2020)报告了5年来其所在实验室碳酸盐矿物的U和Pb含量数据, U和Pb含量平均值分别为1.9和0.003μg g^{-1}. 因此, 学者优先使用高灵敏度的ICP-MS仪器, 如SF-ICP-MS: Thermo Element 2/XR、Nu Plasma 3和Nu Attom ES(Li等, 2014; Roberts等, 2017; Hansman等, 2018; Guillong等, 2020; Hoareau等, 2021). Thermo Element XR型号的SF-ICM-MS可配置高灵敏度Jet采样锥和X截取锥, 使得仪器灵敏度进一步提高, 进而改善分析精度(Hu等, 2012; He等, 2018; Wu等, 2018; Guillong等, 2020; Wu等, 2020a; Yang等, 2020; 杨岳衡等, 2021). Yokoyama等(2018)曾探究了Jet锥和X锥在Neptune Plus MC-ICP-MS仪器上开展方解石U-Pb定年情况. 但由于仪器设计不同, 不同仪器使用相同锥的效果可能不一样. 目前尚未见文献报道过Jet锥和X锥在Element XR仪器开展方解石U-Pb定年的工作.

本文探究了三种锥组合(S+H、Jet+H和Jet+X)在添加和未添加N_2条件下对U和Pb灵敏度的影响, 并系统评估了三个标准物质(NIST SRM 614、ARM-3和WC-1)的激光剥蚀$^{206}Pb/^{238}U$动态分馏情况. 采用一套优化过的仪器参数(Jet+X锥组和添加少量N_2), 本研究分析了四个常用方解石U-Pb定年标准物质(WC-1、Duff Brown Tank、JT和ASH-15), 验证了新研制的ARM-3安山岩玻璃标准物质可用于方解石的$^{207}Pb/^{206}Pb$比值校准. 同时, 进一步证明基于LA-ICP-MS二维元素成像技术辅助选取样品定年区域可有效提高定年成功率, 仅需要增加有限的分析时间和工作量.

2 样品与方法

2.1 样品

本研究共使用6个样品, 包括2个硅酸盐玻璃标准物质和4个方解石U-Pb年龄标准物质. 学者已对这些标准物质开展了系统的表征工作(Jochum等, 2011; Roberts等, 2017; Wu等, 2019, 2021; Guillong等, 2020). 表1汇总了6个标准物质的详细信息.

2.1.1 NIST SRM 614

该样品是人工合成的钠钙质玻璃标准物质, 其微量元素含量在0.8~3.0μg g^{-1}(Jochum等, 2011). 多数实验室采用NIST SRM 614校正方解石$^{207}Pb/^{206}Pb$和$^{208}Pb/^{206}Pb$的仪器分馏. 虽然该玻璃的基体明显不同于方解石, 但测试过程中不同基体的$^{207}Pb/^{206}Pb$比值未见明显的分馏(Guillong等, 2020; Roberts等, 2020).

2.1.2 ARM-3

该样品为新研发的安山岩玻璃标准物质, 其微量元素含量为~5μg g^{-1}. 先前采用不同的分析技术对54种主量和微量元素进行了表征(Wu等, 2019). 最近, Wu等(2021)使用一系列方法对该标准物质的多个同位素比值(Li、B、Si、O、Mg、Sr、Nd、Hf和Pb同位素)进行了表征. 本文评估了采用ARM-3校正方解石$^{207}Pb/^{206}Pb$的适用情况.

2.1.3 WC-1

该样品是海相方解石胶结物, 质量为1kg左右. 取

表 1　本文使用的硅酸盐玻璃Pb-Pb标准物质和方解石U-Pb定年标准物质

名称	基体	采样位置	年龄(Ma)	不确定度(Ma)	U含量 ($\mu g\ g^{-1}$)	表征技术	参考文献
NIST SRM 614	钠钙质玻璃	–	–	–	0.823	ICP-MS	Jochum等, 2011
ARM-3	安山岩玻璃	–	–	–	3.75	ICP-MS	Wu等, 2019
WC-1	海相方解石	美国西德克萨斯州特拉华盆地	254	6.4	~5	ID-TIMS	Roberts等, 2017
Duff Brown	灰岩	美国亚利桑那州科科尼诺高原	64.04	0.67	5~20	ID-MC-ICP-MS	Hill等, 2016
JT-1	方解石	瑞士北部磨拉石盆地	13.797	0.031	~0.5	ID-TIMS	Guillong等, 2020
ASH-15D	方解石	以色列南部内盖夫沙漠喀斯特洞穴	2.965	0.011	2~5	ID-TIMS	Nuriel等, 2021

自二叠纪(Capitanian阶)生物礁内，充填于断层的不整合海相岩脉，出露在位于西德克萨斯州特拉华盆地西侧的瓜达卢佩山脉上. WC-1的ID-TIMS U-Pb年龄为(254.4±6.4)Ma(2s)，放射成因Pb含量为85~98%(Roberts等，2017)，U含量为5μg g^{-1}左右. WC-1是目前唯一一个详细表征、并广泛分发于LA-ICP-MS实验室的方解石U-Pb定年标准物质.

2.1.4　Duff Brown Tank

该样品是在Duff Brown Tank采集的，Duff Brown Tank地层是富黏土粉砂岩中粗粒长石砂岩透镜体与Long Point石灰岩互层. Long Point石灰岩是一个位于亚利桑那州威廉姆斯西北60km处的科科尼诺高原上的白色到浅灰色湖相沉积单元. Duff Brown Tank的ID-MC-ICP-MS U-Pb年龄为(64.04±0.67)Ma(Hill等，2016)，U含量为5~20μg g^{-1}.

2.1.5　JT

该样品是个方解石脉，采自于瑞士北部磨拉石盆地的深钻孔，产于中三叠统Mushelkalk群泥晶灰岩中. JT是方解石脉网的一部分，该脉网与侏罗褶皱和逆冲断层带的基底滑脱构造分支的逆冲断层有关. JT的ID-TIMS U-Pb年龄为(13.797±0.031)Ma(Guillong等，2020)，U含量为0.5μg g^{-1}左右.

2.1.6　ASH-15

该样品采自以色列南部内盖夫沙漠中部的喀斯特Ashalim洞穴. 洞穴入口处海拔414m，位于地中海海岸东南67km处. ASH-15未进行U不平衡校正的ID-TIMS U-Pb年龄为(2.965±0.011)Ma(Nuriel等，2021)，是合适的方解石U-Pb定年标准物质，目前已经在几个实验室得到了应用. 但由于其放射性成因Pb含量低，因此需要采用高灵敏仪器(SF-ICP-MS或MC-ICP-MS)进行测试. ASH-15的U含量范围为2~5μg g^{-1}.

2.2　LA-Q-ICP-MS二维元素成像

LA-四极杆(Q)-ICP-MS二维(2D)元素成像分析是在中国科学院地质与地球物理研究所(IGGCAS)进行的. 样品首先制备成直径为2.50或1.25cm的环氧树脂靶，并抛光至样品表面露出. 将树脂靶放置于HelEx-II激光剥蚀池，采用Photo Machine Analyte G2 193nm ArF准分子激光剥蚀系统(Teledyne CETAC，Omaha，USA)与Agilent 7500a Q-ICP-MS(Agilent Technologies，Santa Clara，USA)联用的LA-Q-ICP-MS进行测试. 采集^{24}Mg、^{29}Si、^{43}Ca、^{55}Mn、^{57}Fe、^{69}Ga、^{85}Rb、^{88}Sr、^{90}Zr、^{137}Ba、^{139}La、^{140}Ce、^{141}Pr、^{146}Nd、^{147}Sm、^{153}Eu、^{158}Gd、^{159}Tb、^{163}Dy、^{165}Ho、^{166}Er、^{169}Tm、^{173}Yb、^{175}Lu以及^{206}Pb、^{207}Pb、^{208}Pb、^{232}Th和^{238}U同位素的信号强度. 激光剥蚀频率和能量密度分别为15Hz和~2.0J cm^{-2}，激光剥蚀束斑为50μm，线扫描速度为40~50μm s^{-1}. 采用NIST SRM 614和ARM-3作为元素定量校准标准物质，其参考值取自Jochum等(2011)和Wu等(2019). 采用Iolite软件中的“Trace_Element DRS”和“半定量”校准方法，计算元素含量. 基于Iolite v4软件生成二维元素图像(Paul等，2012; Petrus等，2017). 表2汇总了仪器信息和详细参数.

2.3 LA-SF-ICP-MS U-Pb定年

LA-SF-ICP-MS原位方解石U-Pb定年在中国科学院地质与地球物理研究所(IGGCAS)进行的. 采用Photo Machine Analyst G2激光剥蚀系统与Element XR(Thermo Fisher Scientific, Bremen, Germany)联用的LA-SF-ICP-MS. Element XR配备了大抽速干泵(On-Tool Booster 150, Asslar, Germany), 可使用高性能Jet采样锥. Ar载气中引入少量N_2可提高仪器灵敏度, 并降低氧化物产率(Hu等, 2008). 我们探究了三种不同的锥组合(S+H、Jet+H和Jet+X)在添加和未添加N_2条件下对U和Pb灵敏度的影响. 为了保证灵敏度最佳, 实验过程中使用了铂屏蔽圈(Wu等, 2020b). 采用T形接头将N_2引入到Ar载气中(位于剥蚀池后), 使用MKS GE50流量器(Coastal instruments, Burgaw, NC, USA)对N_2流量进行控制.

实验在全自动化模式下进行, 60~80剥蚀点为一个分析组. 单点分析包括8s的背景信号采集、25s的剥蚀信号采集以及30s的清洗. 数据采集过程中, 采用跳峰方式检测^{202}Hg、^{204}(Hg+Pb)、^{206}Pb、^{207}Pb、^{208}Pb、^{232}Th和^{238}U信号强度, 单次扫描积分时间为0.27s, 单点分析共进行130次扫描. 对于未知样品, 每间隔十个分析点插入两个NIST SRM 614、两个ARM-3和三个方解石标准物质WC-1. 每个未知样品进行30~40点分析. 方解石标准物质Duff Brown Tank、JT和ASH-15被视为未知样品. 详细的仪器参数汇总于表2.

数据处理方法与Roberts等(2017)、Ring和Gerdes (2016)、Hansman等(2018)和Nuriel等(2021)类似, 这里只简要介绍. 将ICP-MS原始数据(同位素信号强度数据)导入到Iolite 3.7处理软件中(Paton等, 2011). 第一步, 采用NIST SRM 614作为标准物质和VisualAge数据处理策略(Petrus和Kamber, 2012), 计算出^{207}Pb/^{206}Pb和^{206}Pb/^{238}U比值及其分析不确定度. 采用Paton等(2010)所描述的方法, 基于NIST SRM 614分馏曲线对WC-1和其他样品的^{206}Pb/^{238}U分馏进行校正. 第二步, 采用基体匹配的WC-1标准物质进一步校正方解石^{238}U/^{206}Pb比值的系统偏差. 这一步是在Microsoft Excel中完成的. 图1展示了方解石的数据处理方法. 在不同分析时间段内校正因子有所变化(详见3.6节讨论). 数据由IsoplotR软件进行画图(Vermeesch, 2018).

3 结果与讨论

3.1 激光剥蚀元素分馏效应

激光剥蚀元素分馏(Laser induced element fractionation, LIEF)定义为随激光剥蚀时间增加, Pb/U比值的变化(Jeffries等, 1998; Jeffries等, 2003). LIEF是影响U-Pb定年精度的主要因素之一. 值得注意的是, 不同实验室观测到的LIEF可能不相同, 并且LIEF也会随激光参数改变而变化(Paton等, 2010). 通常我们采用标准物质来校正这种元素分馏效应(Woodhead和Petrus, 2019).

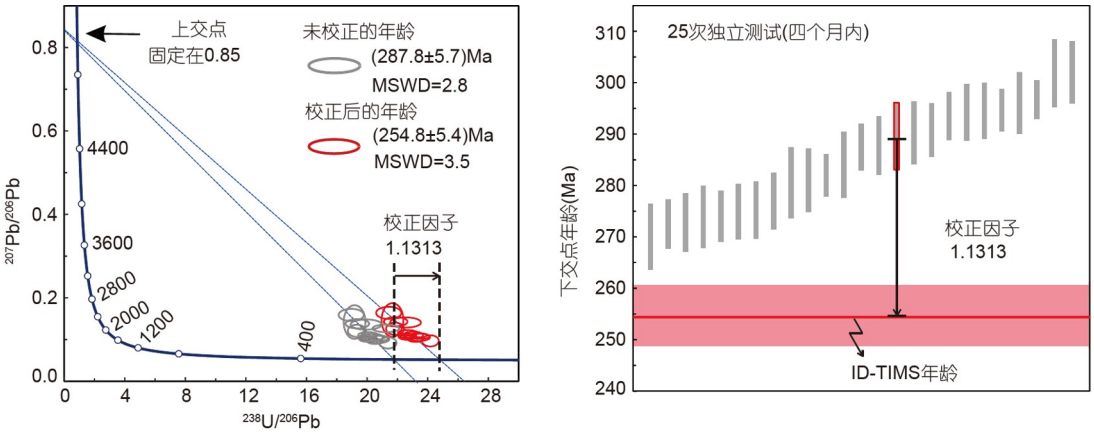

图 1 方解石U-Pb定年的"两步法"校准策略

以Tera-Wasserburg图展示校准流程. 图中"未校正年龄"是指采用NIST SRM 614作为标准物质校正得到的^{207}Pb/^{206}Pb和^{238}U/^{206}Pb年龄. 采用Iolite软件和Microsoft Excel实现校准策略. 4个月共进行了25次独立分析, 校正因子的变化范围为1.063~1.189. 校正因子为NIST SRM 614作为标准物质计算得到的年龄与ID-TIMS推荐年龄之间的偏差系数

表 2　LA-(Q, SF)-ICP-MS二维元素成像和U-Pb定年的仪器参数

	二维元素成像	U-Pb定年
激光剥蚀系统		
厂家与型号	Photon Machines Analyte G2	Photon Machines Analyte G2
激光剥蚀池型号	HelEx 剥蚀池	HelEx 剥蚀池
激光波长	193nm	193nm
激光脉冲	~5ns	~5ns
能量密度	~ 3J cm^{-2}	~ 2J cm^{-2}
剥蚀频率	15或20Hz	8Hz
激光束斑	50μm	85和110μm
采样模式	线扫描速度 40~50m s^{-1}	单点剥蚀, 两个激光脉冲预剥蚀
载气流速(He)	~0.75L min^{-1}	~0.75L min^{-1}
剥蚀时间	随扫描线长度变化而变化	30s
ICP-MS		
厂家与型号	Agilent 7500a	Thermo Element XR
RF功率	1350W	1320W
铂屏蔽圈	未使用	接地
采样锥	镍AT1001-Ni	标准锥、Jet 锥
截取锥	镍AT1002-Ni	H锥、X锥
冷却气流速(Ar)	15.00L min^{-1}	15.00L min^{-1}
辅助气流速(Ar)	0.80L min^{-1}	0.80L min^{-1}
载气流速(Ar)	1.15L min^{-1}	0.95L min^{-1}
增敏气体流速(N_2)	未使用	S+H: 4mL min^{-1}; Jet+H和Jet+X: 6mL min^{-1}
采集模式	跳峰	电场扫描
同位素(m/z)和积分时间(ms)	^{24}Mg(6)、^{29}Si(6)、^{43}Ca(6)、^{55}Mn(6)、^{57}Fe(6)、^{69}Ga(6)、^{85}Rb(6)、^{88}Sr(6)、^{90}Zr(6)、^{137}Ba(6)、^{139}La(6)、^{140}Ce(6)、^{141}Pr(6)、^{146}Nd(6)、^{147}Sm(6)、^{153}Eu(6)、^{158}Gd(6)、^{159}Tb(6)、^{163}Dy(6)、^{165}Ho(6)、^{166}Er(6)、^{169}Tm(6)、^{173}Yb(6)、^{175}Lu(6)、^{206}Pb(15)、^{207}Pb(25)、^{208}Pb(2)、^{232}Th(2)、^{238}U(10)	^{202} Hg(2)、^{204}Pb(2)、^{206}Pb(15)、^{207}Pb (25)、^{208}Pb(2)、^{232}Th(2)、^{238}U(10)
质量窗口	–	20%
单个质量数采集点数	–	20
检测器	SEM(计数与模拟)	SEM(计数和模拟)和法拉第杯
质量分辨率($M/\Delta M$)	~300	~300
单次扫描时间	0.35s	0.27s

在设定的仪器条件下(85μm激光束斑、~2.0J cm^{-2}能量密度和8Hz剥蚀频率下), 我们评估了NIST SRM 614、ARM-3和WC-1的LIEF变化趋势. 图2绘制了NIST SRM 614、ARM-3和WC-1的^{206}Pb/^{238}U LIEF变化趋势图. 红色曲线是12~18个单点测试的平均值, 黑线是LIEF的线性回归结果.

图2中的百分比值是指^{206}Pb/^{238}U比值在激光剥蚀前后的相对变化, 0%表示在剥蚀过程中未发生分馏. 图2显示, 在85μm激光剥蚀束斑、~2.0J cm^{-2}能量密度和8Hz剥蚀频率的参数下, NIST SRM 614、ARM-3和WC-1的LIEF变化不明显, 分别只有0.7%、−2.2%和−1.1%. LIEF不显著, 这可能与采用较大激光束斑(85μm)和较浅剥蚀坑(深度20~30μm)有关. 一般认为低的剥蚀坑深度/束斑比值引起的LIEF比较小. 剥蚀坑

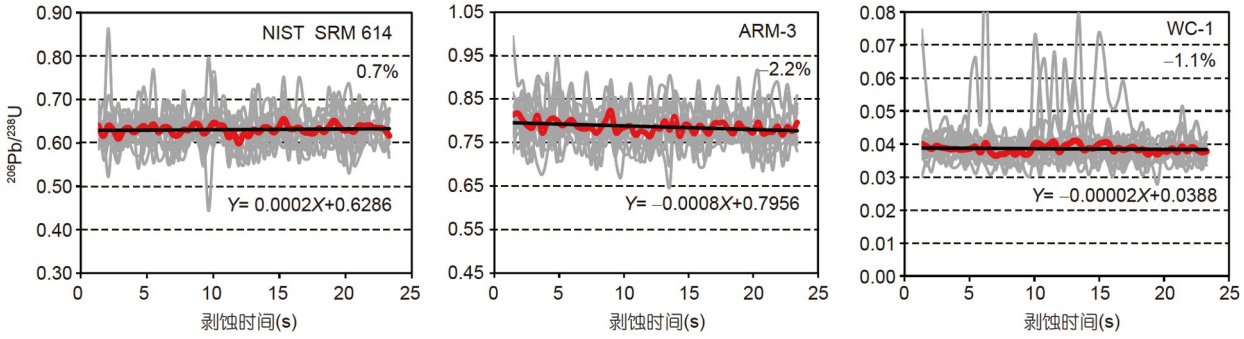

图 2　NIST SRM 614、 ARM-3和WC-1的$^{206}Pb/^{238}U$ 元素分馏(LIEF)情况

激光束斑为85μm、能量密度为~2.0J cm^{-2}、剥蚀频率为8Hz. 三种标准物质的LIFE趋势几乎一致, 变化在2.2%以内

深度是通过剥蚀速率(0.10~0.15μm 脉冲$^{-1}$, 据Wu等(2017))乘以激光脉冲数(200)估算得出的. 若干个WC-1的$^{206}Pb/^{238}U$数据呈现出升高趋势, 可能指示含有普通铅的区域. LIEF对$^{206}Pb/^{238}U$比值的最大不确定度贡献为2.2%. 这个值要小于其他来源的不确定度, 如信号误差和样品不均一等方面. 值得注意的是, 由于仪器类型和激光参数的不同, 本文观测到的LIEF可能与其他实验室不同, 并且会随着激光剥蚀束斑改变而变化, 特别是与之有关的剥蚀坑深度/束斑比值.

3.2　不同锥组合对仪器灵敏度的影响

图3展示了在未添加和添加少量N_2条件下, 三种锥组合(S+H、Jet+H和Jet+X)对^{238}U和^{206}Pb灵敏度的影响. 使用的激光束斑为85μm, 能量密度为~2J cm^{-2}, 剥蚀频率为8Hz. 元素信号强度是在线扫描模式下剥蚀NIST SRM 612采集的. 值得注意的是, 本研究定义的灵敏度是在保持仪器条件ThO^+/Th^+<1.0%和Th^+/U^+比值在0.9~1.1范围内得到的最佳灵敏度. 在三种锥组合中, 引入少量N_2的灵敏度均显著增高, 其中S+H锥组合高3倍左右, Jet+H高1.5倍左右, Jet+X高10倍左右. 我们发现在不加N_2条件下Jet+X锥组的氧化物产率非常高(ThO^+/Th^+ >30%), 但在引入少量N_2后氧化物产率显著降低到1.0%以下. 在未引入少量N_2条件下, Jet+X锥组合灵敏度最低; 在引入少量N_2条件下, 三种锥组合的灵敏度依次为Jet+X>Jet+H > S+H.

与S采样锥相比, Jet采样锥具有较大的孔径. H截取锥和X截取锥的孔径均为0.8mm, 但H锥入口为圆柱型设计, 出口为喇叭型设计, 而X锥则完全是喇叭型设计(Bouman等, 2009). 因此, 与其他锥组合相比, Jet+X

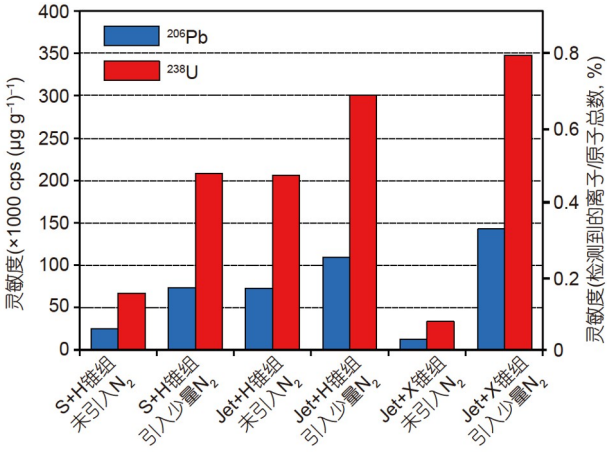

图 3　三种锥组合(S+H、Jet+H和Jet+X)在不引入N_2和引入少量N_2条件下^{206}Pb和^{238}U的信号强度

元素信号强度是在线扫描模式下剥蚀NIST SRM 612采集的, 其中激光束斑85μm、能量密度为~2.0J cm^{-2}、激光频率为8Hz. Jet+X锥组在引入少量N_2条件下^{206}Pb和^{238}U信号强度最高. 灵敏度分别以cps (μg g^{-1})$^{-1}$和检测到的离子数与原子总数比值的形式表示

锥组合能为离子束传输提供更大空间. 这些优点使得Jet+X锥组合具有更高的灵敏度. 如图3所示, 在激光束斑为85μm、能量密度为~2J cm^{-2}、剥蚀频率为8Hz参数下, 采用N_2增敏技术和Jet+X锥组合的^{238}U灵敏度为350,000cps (μg g^{-1})$^{-1}$, 采用Schaltegger等(2015)提出灵敏度的公式(检测到的离子数/原子数总数), 计算得出的灵敏度为0.76%.

为了与已报道的仪器参数对比, 我们重新计算Hansman等(2018)和Ring和Gerdes(2016)报道的数据, 他们采用的是Thermo Element 2仪器和S+H锥组合, 灵敏度分别为0.13%和0.17%. 这仅为本研究采用Element

XR结合Jet+X锥组合的20~30%. 考虑到方解石中U和Pb含量普遍偏低、并且微米尺度内常有环带分布、包裹体相对较多, 因此在保证数据精度的前提下, 应尽可能地采用小束斑. 本研究提高了灵敏度, 这意味着可以使用更小的激光束斑, 有利于拓展方解石U-Pb地质年代学的应用, 如测定微观尺度孔隙胶结物的形成时代.

3.3 Jet+X锥组结合N_2增敏技术对分析精度的改善

JT方解石标准物质的U含量低(~0.5μg g^{-1}), 并且年龄相对年轻(~14Ma). 因此, 本文选取JT来验证高灵敏度对分析结果的优势. 图4比较了三种锥组合(S+H在不引入N_2条件下、Jet+H在不引入N_2条件下, Jet+X在引入少量N_2条件下)的JT分析结果. S+H(不引入N_2)、Jet+H(不引入N_2)、Jet+X(引入少量N_2)的下交点年龄结果, 分别为(15.5±2.3)、(14.4±1.6)和(13.6±0.5) Ma. 虽然年龄与ID-TIMS推荐年龄在误差范围内一致((13.797±0.031)Ma; Guillong等, 2020), 但是Jet+X锥组和N_2增敏技术对数据的内精度(以图中圆圈的大小表示)和下交点年龄精度具有明显改善. Jet+X锥组和N_2增敏技术提高了仪器灵敏度, 这能明显改善对低含量样品的检测能力, 进而改善了分析精度和准确度.

3.4 采用NIST SRM 614和ARM-3对$^{207}Pb/^{206}Pb$的校正

图5a绘制了NIST SRM 614和ARM-3的$^{207}Pb/^{206}Pb$分析精度与^{207}Pb信号强度的关系图. 与NIST SRM 614的Pb含量(2.32μg g^{-1})相比, ARM-3的Pb含量(12.7μg g^{-1})高. 在相同的仪器参数条件下, Pb含量高的样品, ^{207}Pb信号强度更高, 因此ARM-3可能更适用于$^{207}Pb/^{206}Pb$比值的校准. 图5b展示了分别采用NIST SRM 614和ARM-3校准WC-1、Duff Brown Tank、JT和ASH-15的$^{207}Pb/^{206}Pb$比值结果. 结果显示二者不存在明显差异, 表明在校正$^{207}Pb/^{206}Pb$ 比值时, NIST SRM 614与ARM-3之间不存在基体效应. ARM-3的U含量适中, 为~3.75μg g^{-1}, 这与WC-1方解石相似. 参照本研究采用的Element XR灵敏度, 在85μm激光束斑, ~2.0J cm^{-2}能量密度和8 Hz剥蚀频率下, ARM-3的^{238}U的信号强度应该大于1百万cps. 综上所述, ARM-3既可用作$^{207}Pb/^{206}Pb$比值校准, 又可用于方解石U-Pb定年仪器参数优化. 目前ARM-3的$^{206}Pb/^{238}U$比值尚未进行ID-TIMS表征. 进一步表征后, ARM-3可像NIST SRM 614一样用作$^{206}Pb/^{238}U$比值校准标准物质.

3.5 激光二维元素成像

通常方解石的元素含量在微米尺度上是变化的(Roberts等, 2020; Rasbury等, 2021). 因此, 二维元素成像能为探究岩石成因和蚀变过程提供重要信息, 同时也能为选取适合定年的高U区域提供重要参考(Roberts等, 2020). 先前已有学者对WC-1开展了二维元素成像(Roberts等, 2017), 但手标本之间可能会不同. 如Guillong等(2020)报道, 他们的WC-1中较暗部分的U-Pb年龄结果与推荐年龄((254.4±6.4)Ma)一致, 而较亮

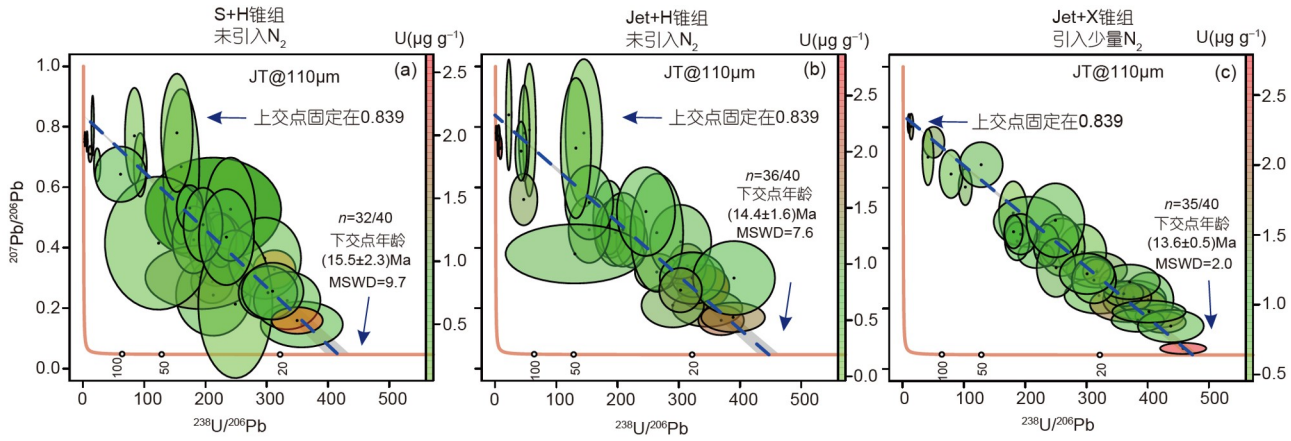

图 4 不同条件下JT年龄结果的Tera-Wasserburg图

(a) S+H, 不引入N_2; (b) Jet+H, 不引入N_2; (c) Jet+X, 引入少量N_2. $^{207}Pb/^{206}Pb$锚点固定为0.839(Guillong等, 2020). 采用高灵敏度Je t+X锥组和N_2增敏技术明显改善了分析结果的精度和准确度. 少数的分析数据为异常值. 图中的*n*=*a*/*b*, 其中"*a*"表示剔除异常值的数据总数, "*b*"表示分析总次数

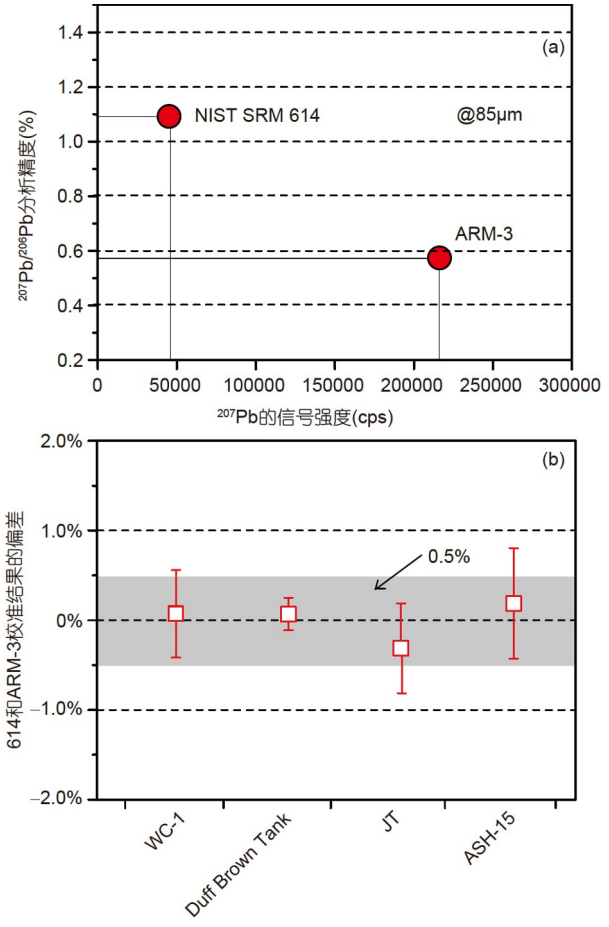

图 5　NIST SRM 614与ARM-3分析结果

(a) NIST SRM 614和ARM-3的^{207}Pb/^{206}Pb分析精度与^{207}Pb信号强度的关系图; (b) 分别采用NIST SRM 614和ARM-3校正的WC-1、Duff Brown Tank、JT和ASH-15的^{207}Pb/^{206}Pb结果. 偏差为(1~614校正数据/ARM-3校正数据)×100. 数据表明, 在进行^{207}Pb/^{206}Pb 校正时, NIST SRM 614与ARM-3之间不存在基体效应

的脉状部分年龄分散、并且要年轻((202.9±6.9)Ma). 因此, 有必要对每一块WC-1标准物质进行评估(如采用二维元素成像技术), 这主要是因为方解石常常伴有元素含量和同位素比值不均一的现象. Duff Brown Tank曾作为标样用于开发U-Pb年代学成像技术(Drost等, 2018). 本文系统探究了WC-1、Duff Brown Tank和JT的元素二维分布情况.

如图6所示, 三个标准物质的元素含量在微米尺度上呈出明显不均一. 对于WC-1和Duff Brow Tank来说, U含量与轻稀土La呈正相关, 而与Sr或Mg无关. WC-1中的Sr含量明显高于Duff Brown Tank和JT, 指示WC-1可能是一个潜在的原位Sr同位素分析标准物质(Rasbury等, 2021). 对于JT来说, 元素特征明显分成了两部分, 右半部分为围岩, Mg、Sr、La和U含量较高, 左侧为方解石脉, 其推荐年龄为(13.797±0.031)Ma. 综合上述结果, 我们建议对每个方解石标准物质, 应进行二维元素成像分析, 这样可以更好地评估其质量.

3.6　WC-1、Duff Brown Tank、JT和ASH-15的U-Pb年龄结果

3.6.1　WC-1

在本研究中, 该样品作为U-Pb定年标准物质, 因此不能用来评估方法的准确性. 在4个月时间内, 我们共对WC-1进行了25次独立分析. 结果汇总于图1. 在这25次独立分析中, 激光束斑和剥蚀频率均保持一致, 我们发现校正因子并不是固定不变的, 而是在1.063~1.189变化, 这可能与仪器调试状态有关.

3.6.2　Duff Brown Tank

这个样品共进行了四次分析(三次使用85μm激光束斑, 一次使用50μm激光束斑, 如图7所示). 分别以不固定上交点和固定上交点绘制了Tera-Wasserburg图(数据见网络版附表1, http://earthcn.scichina.com). 对于固定上交点的结果, 我们将^{207}Pb/^{206}Pb 固定在0.738 (Hill等, 2016). 该样品的普通铅含量为18.6%~86.7%. 对于绝大多数单点分析, 其^{238}U/^{206}Pb分析精度优于4.0%(2SE), ^{207}Pb/^{206}Pb分析精度优于3.0%(2SE). 四次分析得到的U含量平均值为(15.1±9.4)μg g^{-1}. 不固定上交点的四次年龄结果分别为(62.1±1.5)、(62.7±1.5)、(64.4±1.1)和(63.8±1.7)Ma, 这要比之前报道的ID-TIMS年龄((64.04±0.67)Ma)稍微偏低一些, 但考虑到分析误差, 总体上也是一致的. 拟合在Y轴的^{207}Pb/^{206}Pb比值(0.662~0.698)也是明显低于报道值(0.738±0.01; Hill等, 2016). 四次实验均发现这种偏低的现象(图7).

上交点固定的四次年龄结果分别为: (65.5±0.6)、(66.7±0.7)、(66.6±0.6)和(65.8±0.5)Ma, 这要比之前报道的ID-TIMS年龄((64.04±0.67)Ma)稍微偏老一些, 考虑到LA-ICP-MS方解石U-Pb定年的误差(3.5%), 总体上也可以认为是一致的. 相比于未固定上交点的数据, 固定上交点的MSWD变大了. 对于固定上交点的数据, 如果是因为校正问题导致的^{238}U/^{206}Pb和^{207}Pb/^{206}Pb系统偏差, 等时线将会在Tera-Wasserburg图中平行移动, 也就是说, 如果我们将未固定上交点的等时线平行移

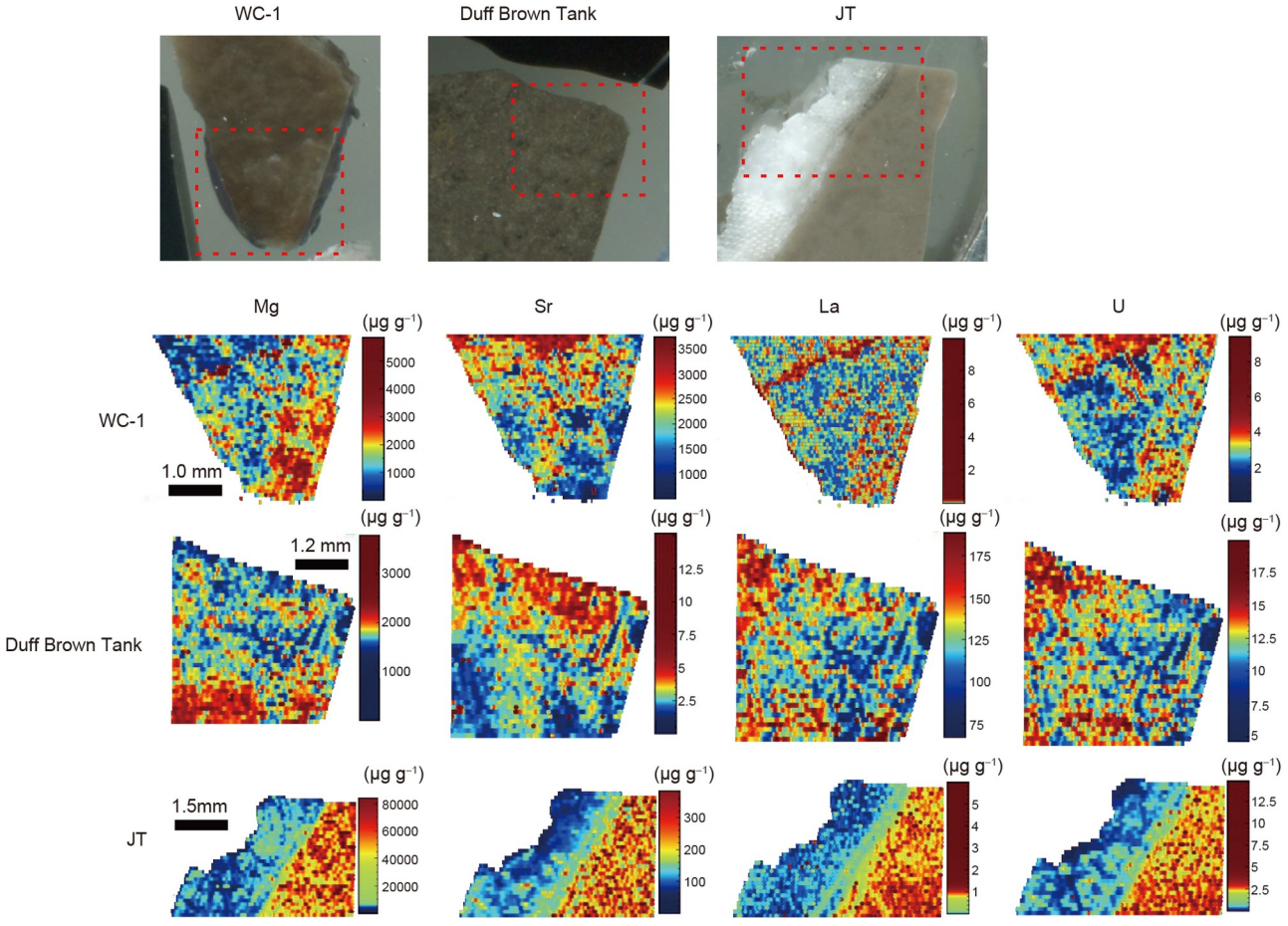

图 6　WC-1、Duff Brown Tank和JT的Mg、Sr、La和U的二维元素成像图

最上行是光学显微镜图片. 元素含量单位以μg g^{-1}表示. 结果显示Mg、Sr、La和U在微米尺度上不均一

动到Y轴交点$^{207}Pb/^{206}Pb$=0.738，那么此时的下交点年龄将会变的更年轻, 这表明我们实验测出的$^{207}Pb/^{206}Pb$初始值(0.662~0.698)偏低并不是因为数据校正的问题导致的. 为了进一步证明该推断，我们采用LA-MC-ICP-MS(瑞索M50型号激光剥蚀系统与Neptune Plus MC-ICP-MS联用)对Duff Brown Tank进行了分析(Zhang等，2021). 结果(见网络版附图1)和本研究采用LA-SF-ICP-MS的结果一致, 这表明Duff Brown Tank的初始$^{207}Pb/^{206}Pb$比值可能是不均一的. 值得强调的是, 对于Duff Brown Tank, 虽然我们使用的激光束斑为85和50μm，但由于其Pb和U含量相对较高，空间分辨率是可以降低到50μm以下的.

3.6.3　JT

该样品共进行了两次分析，数据汇总于网络版附表2中, 图8绘制了其Tera-Wasserburg图. 第一次测试是JT方解石脉，上交点$^{207}Pb/^{206}Pb$固定于0.839(Guillong等，2020)，下交点年龄为(13.76±0.43)Ma，这与Guillong等(2020)报道的ID-TIMS年龄((13.797±0.031)Ma)一致. 第二次测试是JT围岩, 因没有合适的参考值, 故未固定上交点, 下交点年龄为(151.5±13.7)Ma. 据我们所知, 这是首次报道JT围岩的U-Pb年龄结果. 如图8所示, 方解石矿脉中的U含量为(0.56±1.00)μg g^{-1}, 围岩中的U含量为(0.88±0.34)μg g^{-1}. 围岩的普通铅组分占比大, 而方解石脉的普通铅占比变化相对较大.

3.6.4　ASH-15

该样品进行了两次分析，数据汇总于网络版附表3，图9绘制了其Tera-Wasserburg图. 对于第一次测试, 当上交点固定时($^{207}Pb/^{206}Pb$: 0.832)，下交点年龄为

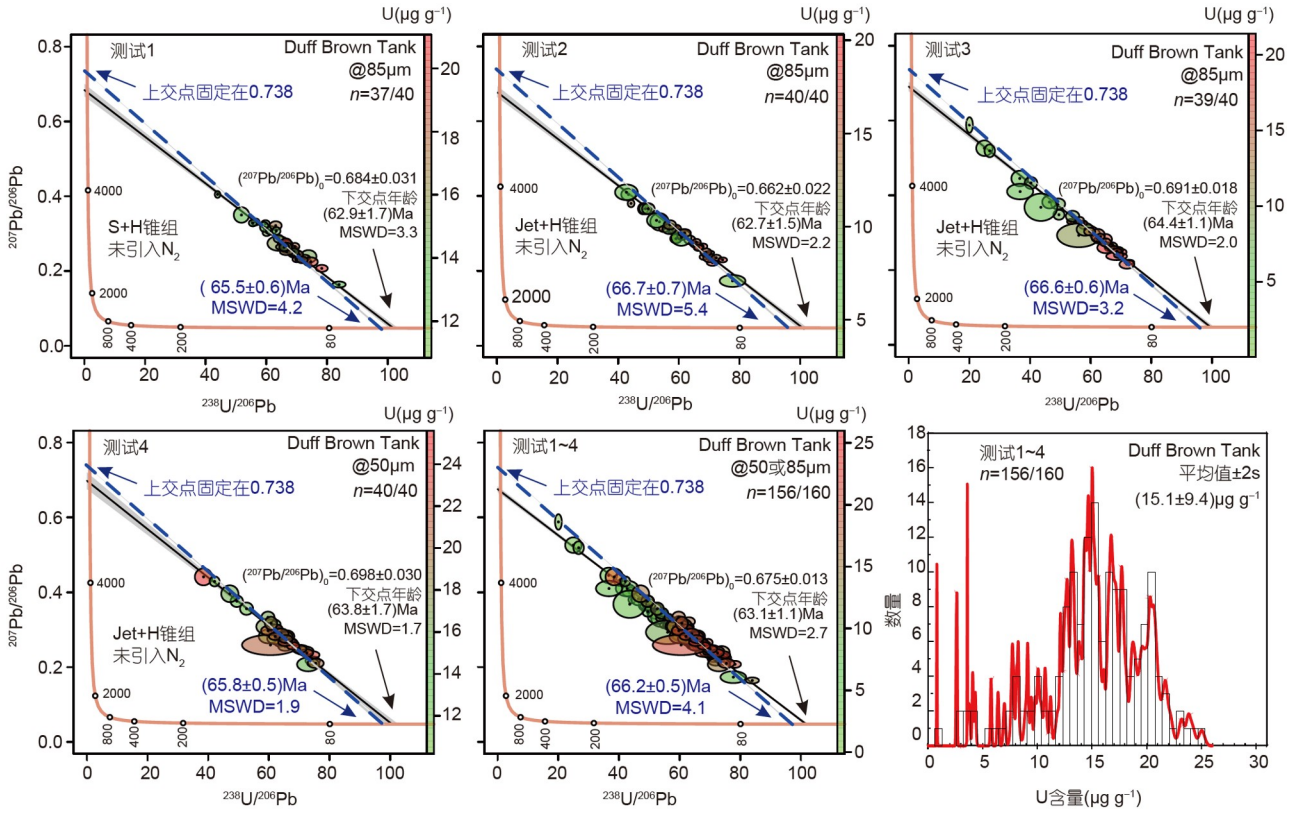

图 7　Duff Brown Tank的LA-SF-ICP-MS数据Tera-Wasserburg图

蓝色虚线为上交点$^{207}Pb/^{206}Pb$固定在0.738(Hill等, 2016)的等时线; 黑色实线为上交点未固定的等时线. U含量变化以相对概率的形式表示. 在不同时间内共进行了4次独立分析, 其中第1~3次的激光束斑为85μm, 第4次激光束斑为50μm. 第1次采用S+H锥组和未引入N_2的仪器条件, 第2~4次采用Jet+X锥组和未引入N_2的仪器条件. 少数分析数据为异常值. 图中的$n=a/b$, 其中"a"表示剔除异常值的数据总数, "b"表示分析总次数. 由IsoplotR软件进行画图(Vermeesch, 2018)

(2.947±0.063)Ma, 当上交点未固定时, 年龄为(2.987±0.080)Ma, 初始$^{207}Pb/^{206}Pb$比值为0.860±0.035. 在误差范围内, 固定和未固定上交点的年龄均与推荐的ID-TIMS年龄((2.965±0.011)Ma; Nuriel等, 2021)一致. 第二次测试, 当上交点固定时($^{207}Pb/^{206}Pb$: 0.832), 下交点年龄为(3.037±0.067)Ma; 当上交点未固定时, 年龄为(3.044±0.075)Ma, 初始$^{207}Pb/^{206}Pb$比值为0.840±0.034. 这两个年龄比ID-TIMS推荐值偏大2.7%左右. 考虑到基体匹配问题、标准物质定值误差以及仪器长期稳定性, LA-ICP-MS方解石定年的不确定度相对较大(3.5%)(Guillong等, 2020; Nuriel等, 2019). 两次ASH-15的测试, 得到的U含量平均值为(1.62±0.91)μg g^{-1}. 虽然ASH-15的年龄小, 但其U含量相对较高. 相比于JT, ASH-15可能容易测一些. 本次测试^{207}Pb的背景为~17.6cps, WC-1(85μm)、ASH-1(110μm)和JT(110μm)的^{207}Pb的信号强度分别为1295~3388、28~1871和136~591cps.

3.7　方解石U-Pb定年的启示

3.7.1　ICP-MS仪器的选择

目前, 已有文献报道采用三种类型的仪器进行方解石U-Pb定年, 包括Q-ICP-MS、SF-ICP-MS和MC-ICP-MS(Kylander-Clark, 2020; 见网络版附表1). 在这三种类型的仪器中, MC-ICP-MS灵敏度最高, 比SF-ICP-MS高3~5倍, 比Q-ICP-MS高10倍以上. 高灵敏度对于测定低含量U或者年轻的样品具有优势. MC-ICP-MS另一个优点是同位素的同时测量, 这能消除由于ICP波动导致的信号不稳定. 但是, MC-ICP-MS仪器昂贵, 普及率不高. MC-ICP-MS通常采用法拉第杯检测大于5mV(1mV=62500cps)的信号, 离子计数器检测小

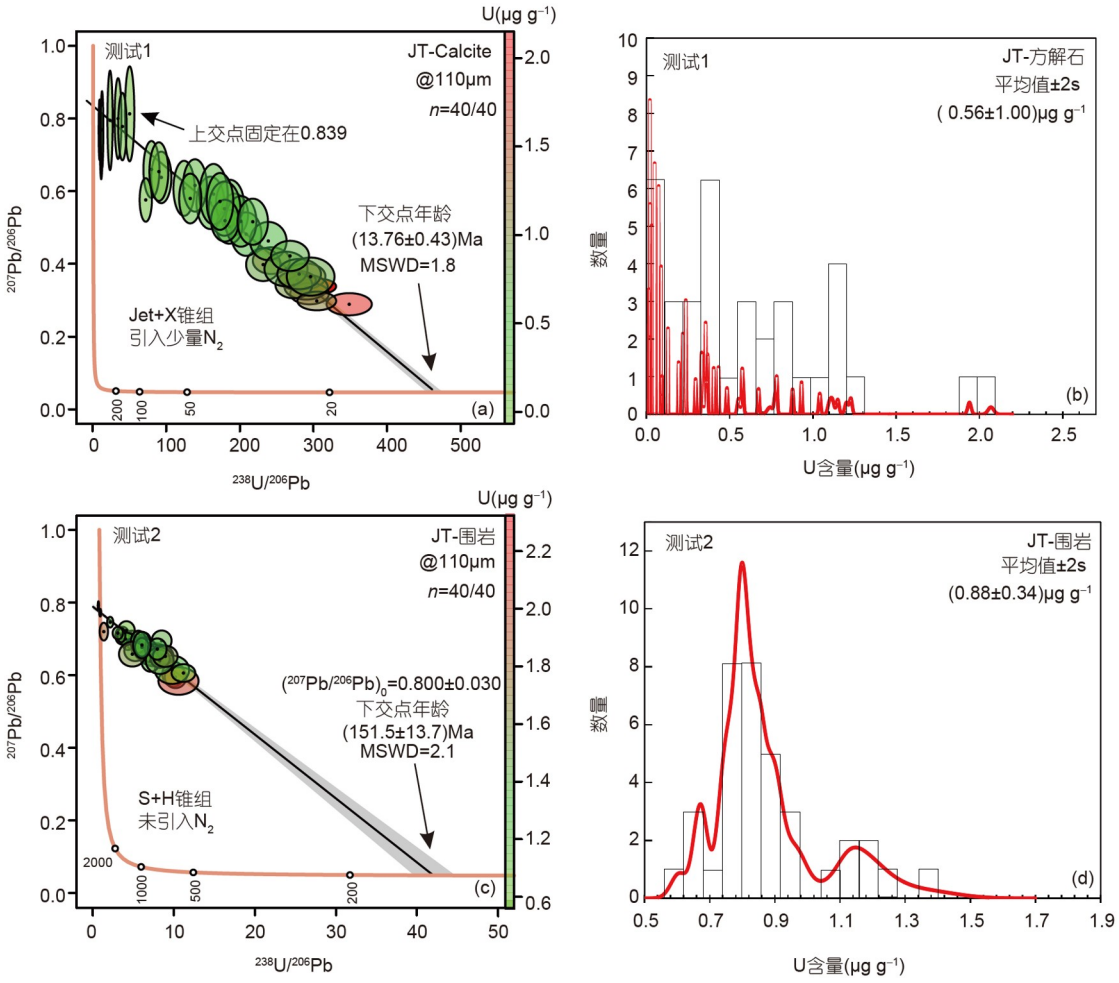

图 8　JT的LA-SF-ICP-MS数据Tera-Wasserburg图

U含量以相对概率的形式表示. 共进行了两次测试, 激光束斑为110μm. 第1次测试((a)、(b))是方解石脉(图6中JT显微镜图左侧白色部分)), 上交点固定为0.839(Guillong等, 2020), 采用了Jet+X锥组和引入少量N_2的仪器条件; 第2次((c)、(d))是围岩(图6中JT显微镜图右侧深色部分), 没有固定上交点, 采用了S+H锥组和未引入N_2的仪器条件. 少数的分析数据为异常值. 图中的$n=a/b$, 其中"a"表示剔除异常值的数据总数, "b"表示分析总次数. 由IsoplotR软件进行画图(Vermeesch, 2018)

于2,000,000cps的信号. 因为方解石中的U和Pb含量变化较大, 因此一套杯结构不能完全满足所有的样品. 此外法拉第杯与离子计数器之间需要交叉校准, 这可能会导致额外的不确定度.

SF-ICP-MS和Q-ICP-MS都是采用单个接收器顺序接收不同元素的信号. 通常是采用二次电子倍增器(SEM), 有的仪器也用法拉第杯. 由于只使用一个二次电子倍增器, 不需要复杂的离子计数器校准, 这使得数据处理相对简单, 仪器维护相对便宜. 一些学者采用法拉第杯, 这能扩大动态检测范围. SF-ICP-MS和Q-ICP-MS的另一个优势是, 在测定U-Pb年龄的同时, 还能测定微量元素(Drost等, 2018). 与MC-ICP-MS相比, Q-ICP-MS和SF-ICP-MS的灵敏度较低, 因此在进行方解石U-Pb定年时, 需要的激光束斑较大. 从网络版附表4可知, Q-ICP-MS激光束斑通常大于200μm, SF-ICP-MS为100~200μm, MC-ICP-MS为100μm左右. 本研究表明相比于已发表的SF-ICP-MS仪器(Element 2和Nu Attom), Element XR采用Jet+X锥和N_2增敏技术, 可以显著提高灵敏度, 从而提高分析的空间分辨率(对大多数方解石, 可以采用50~110μm的激光束斑).

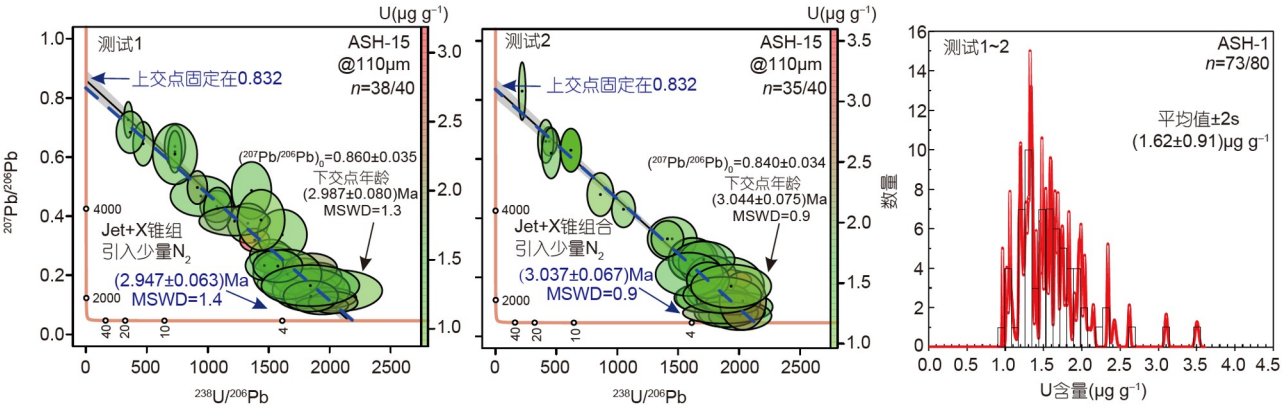

图 9　ASH-15的下交点年龄和U含量结果图

其中下交点年龄结果以Tera-Wasserburg图表示; U含量变化以相对概率的形式表示. 蓝色虚线为固定上交点$^{207}Pb/^{206}Pb$为0.832(Nuriel等, 2021)的等时线; 黑色实线为未固定上交点的等时线. 在不同时间内, 共进行了2次独立分析, 所用激光束斑为110μm和Jet+X锥组和引入少量N_2的仪器条件. 少数的分析数据为异常值. 图中的$n=a/b$, 其中"a"表示剔除异常值的数据总数, "b"表示分析总次数. 数据由IsoplotR软件进行画图(Vermeesch, 2018).

3.7.2　二维元素成像辅助U-Pb定年

由于缺乏直接判别方解石U含量和普通铅含量的标准, 因此很难快速筛选出高U和低普通Pb的样品进行U-Pb定年分析(Roberts等, 2020; Rasbury等, 2021). 在很多地质环境中, 尚不清楚方解石中U的赋存机理, 这主要是因为方解石中的微量元素赋存并不是仅由热力学控制的, 还受到其他参数的影响, 包括微量元素的活度、方解石生长速率、温度、pH值、Eh值、pCO_2、流体的Ca^{2+}/CO_3^{2-}比值、离子半径以及U络合情况等(Roberts等, 2020). 目前, 一些学者已将多种非破坏性成像技术应用于样品筛选, 包括光学显微镜、阴极发光(CL)、电荷造影、背散射电子成像(BSE)和X射线荧光光谱(XRF)成像(Roberts等, 2020; Rasbury等, 2021). 一般认为, 这些技术主要用于识别和表征方解石的生长阶段或蚀变情况, 而难以用来识别高U和低普通Pb区域.

已有研究通常是通过监控^{204}Pb或^{238}U信号强度, 采用点剥蚀或线扫描来筛选高U和低普通Pb区域, 并将这些区域标记下来, 然后进行U-Pb定年(点筛选方法). 另一种方法是采用LA-ICP-MS二维元素成像技术来识别未知样品U和Pb变化区域, 并标记出适合定年的区域, 即"二维元素成像辅助U-Pb定年"方法(Roberts等, 2020). 点筛选法可快速筛选多个样品, 而二维元素成像能为复杂不均一的样品提供更详细的信息. 在本研究中, 我们基于一个未知样品, 比较了这两种方法的优缺点, 数据汇总于网络版附表5. 图10a和10b为使用"点筛选方法"的结果, 图10c和10d为使用"二维元素成像辅助U-Pb定年方法"的结果. 显然, 二维元素成像辅助U-Pb定年方法的结果更好, 这是因为对高U区域的准确定位. 在保证空间分辨率的前提下, 采用我们的激光剥蚀参数, 对面积为5mm×5mm的区域成像仅需要60min.

3.7.3　标准物质的研发

LA-ICP-MS方解石U-Pb定年需要基体匹配的标准物质来校正$^{206}Pb/^{238}U$的仪器分馏. 目前, 一些实验室的内部标样已被用作标准物质, 包括Duff Brown Tank、ASH-15、JT和AHX-1A. 尽管ASH-15进行了ID-TIMS表征, 并已分发到一些实验室, WC-1(ID-TIMS推荐年龄: (254.4±6.5)Ma)仍是应用最多的方解石U-Pb定年标准物质. 但WC-1的年龄不确定度(2.5%)相对较大, 这使得当采用WC-1为标准物质时, 其对未知样品U-Pb年龄校正的最小不确定度贡献为2.5%. 需要注意的是, 一些学者发现WC-1可能是不均一的(Guillong等, 2020); 而且, 某些WC-1标样的Pb/U比值可能比Roberts等(2017)报道的结果变化大. 网络版附表6汇总了一些常用方解石U-Pb定年标准物质, 包括实验室因方法建立而用到的样品. 这其中绝大多数的样品都还没有进行ID-TIMS表征, 目前仅在实验室内

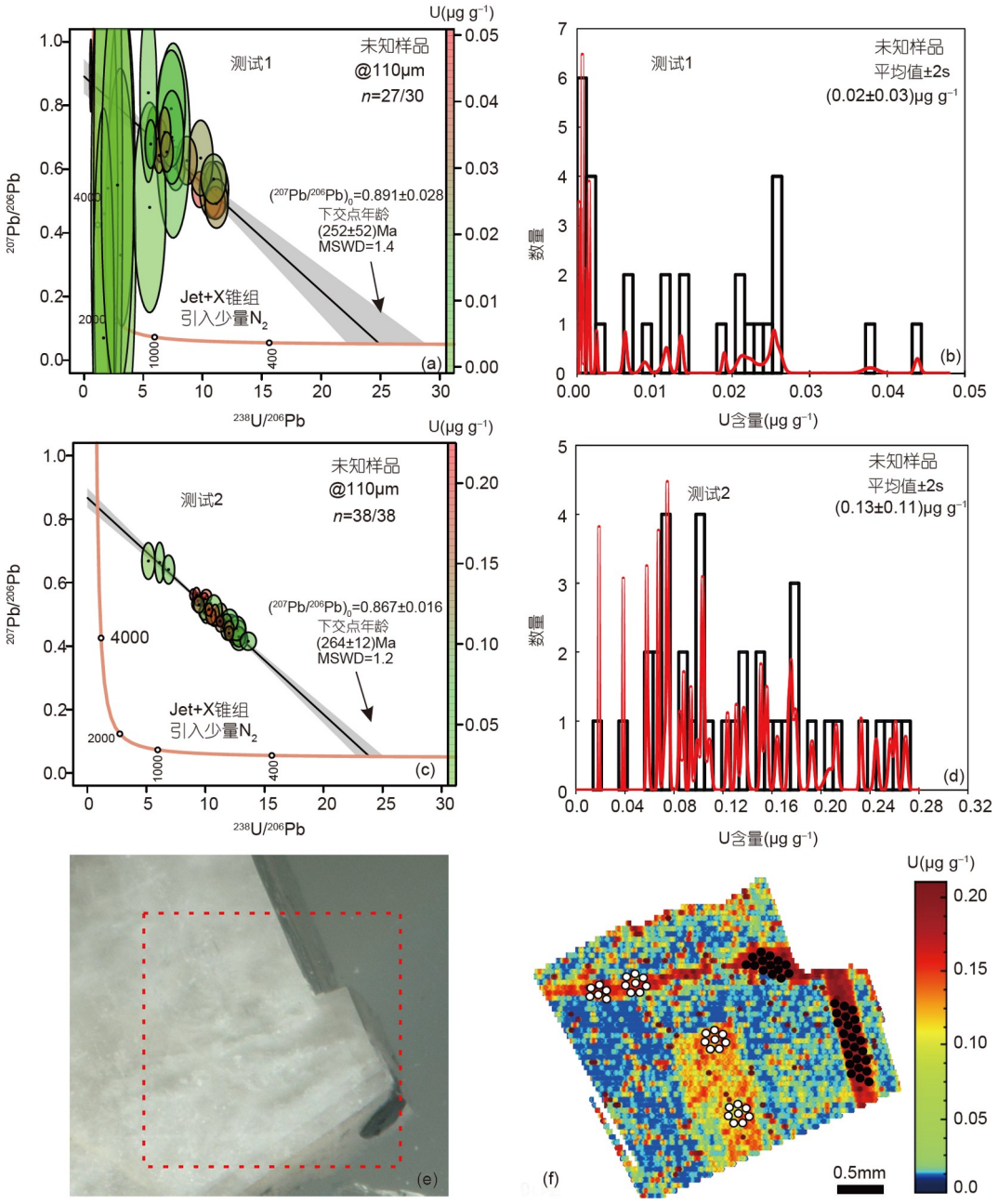

图 10　采用“点筛选”和“二维元素成像辅助U-Pb定年”方法对一个样品的分析结果对比

(a)和(b)为“点筛选”方法分析结果(测试1), 采用了S+H锥组和引入少量N_2的仪器条件, 分析位置见(f)中空心圆; (c)和(d)为“二维元素成像辅助U-Pb定年”方法分析结果(测试2), 采用了Jet+X锥组和引入少量N_2的仪器条件, 分析位置见(f)中实心圆; (e)为光学显微镜下图片. 测试1和测试2均没有剔除异常点, 数据由IsoplotR软件进行画图(Vermeesch, 2018)

部使用.

LA-ICP-MS方解石U-Pb定年的技术瓶颈仍然是缺乏基体匹配标准物质. 特别是碳酸盐岩矿物具有多样性, 如不同矿物类型(方解石、白云石和文石)、化学组成(高镁方解石)以及U-Pb年龄差别(如年轻样品中的低放射性铅). 标准物质和未知样品间的基体差异(如微晶、细晶和粗晶的差别), 会导致不同的剥蚀效率、元素分馏以及剥蚀坑深度, 进而会增加U-Pb定年

的不确定性(Elisha等, 2021). 剥蚀坑深度差别可能会导致下交点年龄偏差高达20%(Guillong等, 2020). 目前已有的标准物质不能满足应用需求, 特别是白云石和霰石等.

4 结论

激光剥蚀电感耦合等离子体质谱(LA-ICP-MS)方解石U-Pb年代学是新兴的地质定年技术, 具有解决关键地质问题的潜力. 由于方解石的U和Pb含量低, 因此通常采用灵敏度高的仪器, 如扇形磁场(SF)ICP-MS, 进行方解石U-Pb定年测试. 我们采用Thermo Element XR仪器, 发现当采用Jet+X锥和N_2增敏时, U和Pb灵敏度最佳. 高灵敏度能改善低U含量和低放射性成因Pb样品的分析精度和准确度, 同时提高空间分辨率至<100μm. 在剥蚀坑深度/束斑比值小的情况下, NIST SRM 614、ARM-3和WC-1标样的激光剥蚀$^{206}Pb/^{238}U$分馏不显著(<2.2%). 采用最优的仪器参数, 以WC-1为标准物质, 本文系统分析了三个常用方解石U-Pb标准物质(Duff Brown Tank、JT和ASH-15), 所得结果与ID-TIMS推荐年龄相吻合, 证明了我们技术的可靠性. 此外, 我们还表明ARM-3标准物质可用于方解石的$^{207}Pb/^{206}Pb$校正和仪器参数优化, 基于LA-ICP-MS二维元素成像技术选取样品定年区域可提高定年的成功率.

致谢 感谢Perach NURIEL、Victor POLYAK和Marcel GUILLONG提供的方解石U-Pb标准物质ASH-15、Duff Brown Tank和JT. 感谢马红霞对样品的前处理工作和张亮亮提供的LA-MC-ICP-MS数据.

参考文献

杨岳衡, 杨明, 王浩, 杨进辉, 吴福元. 2021. 黑钨矿微区原位U-Pb年代学方法及应用. 中国科学: 地球科学, 51: 171–174

Bouman C, Deerberg M, Schwieters J. 2009. NEPTUNE and NEPTUNE Plus: Breakthrough in Sensitivity using a Large Interface Pump and New Sample Cone. Thermo Fischer Scientific Application Note: 30187, https://www.analyteguru.com/t5/Scientific-Library/NEPTUNE-and-NEPTUNE-Plus-Breakthrough-in-Sensitivity-using-a/ta-p/4994

Burisch M, Gerdes A, Walter B F, Neumann U, Fettel M, Markl G. 2017. Methane and the origin of five-element veins: Mineralogy, age, fluid inclusion chemistry and ore forming processes in the Odenwald, SW Germany. Ore Geol Rev, 81: 42–61

Cheng T, Zhao J, Feng Y, Pan W, Liu D. 2020. *In-situ* LA-MC-ICPMS U-Pb dating method for low-uranium carbonate minerals. Chin Sci Bull, 65: 150–154

Coogan L A, Parrish R R, Roberts N M W. 2016. Early hydrothermal carbon uptake by the upper oceanic crust: Insight from *in situ* U-Pb dating. Geology, 44: 147–150

Drost K, Chew D, Petrus J A, Scholze F, Woodhead J D, Schneider J W, Harper D A T. 2018. An image mapping approach to U-Pb LA-ICP-MS carbonate dating and applications to direct dating of carbonate sedimentation. Geochem Geophys Geosyst, 19: 4631–4648

Elisha B, Nuriel P, Kylander-Clark A, Weinberger R. 2021. Towards *in situ* U-Pb dating of dolomite. Geochronology, 3: 337–349

Engel J, Maas R, Woodhead J, Tympel J, Greig A. 2020. A single-column extraction chemistry for isotope dilution U-Pb dating of carbonate. Chem Geol, 531: 119311

Goodfellow B W, Viola G, Bingen B, Nuriel P, Kylander-Clark A R C. 2017. Palaeocene faulting in SE Sweden from U-Pb dating of slickenfibre calcite. Terra Nova, 29: 321–328

Guillong M, Wotzlaw J F, Looser N, Laurent O. 2020. Evaluating the reliability of U-Pb laser ablation inductively coupled plasma mass spectrometry (LA-ICP-MS) carbonate geochronology: Matrix issues and a potential calcite validation reference material. Geochronology, 2: 155–167

Hansman R J, Albert R, Gerdes A, Ring U. 2018. Absolute ages of multiple generations of brittle structures by U-Pb dating of calcite. Geology, 46: 207–210

He T, Ni Q, Miao Q, Li M. 2018. Effects of cone combinations on the signal enhancement by nitrogen in LA-ICP-MS. J Anal At Spectrom, 33: 1021–1030

Hill C A, Polyak V J, Asmerom Y, P. Provencio P. 2016. Constraints on a Late Cretaceous uplift, denudation, and incision of the Grand Canyon region, southwestern Colorado Plateau, USA, from U-Pb dating of lacustrine limestone. Tectonics, 35: 896–906

Hoareau G, Claverie F, Pecheyran C, Paroissin C, Grignard P A, Motte G, Chailan O, Girard J P. 2021. Direct U-Pb dating of carbonates from micron-scale femtosecond laser ablation inductively coupled plasma mass spectrometry images using robust regression. Geochronology, 3: 67–87

Holdsworth R E, McCaffrey K J W, Dempsey E, Roberts N M W, Hardman K, Morton A, Feely M, Hunt J, Conway A, Robertson A. 2019. Natural fracture propping and earthquake-induced oil migration in fractured basement reservoirs. Geology, 47: 700–704

Hu Z, Liu Y, Gao S, Liu W, Zhang W, Tong X, Lin L, Zong K, Li M, Chen H, Zhou L, Yang L. 2012. Improved *in situ* Hf isotope ratio

analysis of zircon using newly designed X skimmer cone and jet sample cone in combination with the addition of nitrogen by laser ablation multiple collector ICP-MS. J Anal At Spectrom, 27: 1391–1399

Hu Z, Gao S, Liu Y, Hu S, Chen H, Yuan H. 2008. Signal enhancement in laser ablation ICP-MS by addition of nitrogen in the central channel gas. J Anal At Spectrom, 23: 1093–1101

Jahn B, Cuvellier H. 1994. Pb-Pb and U-Pb geochronology of carbonate rocks: An assessment. Chem Geol, 115: 125–151

Jeffries T E, Fernandez-Suarez J, Corfu F, Gutierrez Alonso G. 2003. Advances in U-Pb geochronology using a frequency quintupled Nd: YAG based laser ablation system (λ= 213 nm) and quadrupole based ICP-MS. J Anal At Spectrom, 18: 847–855

Jeffries T E, Jackson S E, Longerich H P. 1998. Application of a frequency quintupled Nd: YAG source (λ=213 nm) for laser ablation inductively coupled plasma mass spectrometric analysis of minerals. J Anal At Spectrom, 13: 935–940

Jochum K P, Weis U, Stoll B, Kuzmin D, Yang Q, Raczek I, Jacob D E, Stracke A, Birbaum K, Frick D A, Günther D, Enzweiler J. 2011. Determination of reference values for NIST SRM 610-617 glasses following ISO guidelines. Geostand Geoanal Res, 35: 397–429

Kurumada Y, Aoki S, Aoki K, Kato D, Saneyoshi M, Tsogtbaatar K, Windley B F, Ishigaki S. 2020. Calcite U-Pb age of the Cretaceous vertebrate-bearing Bayn Shire Formation in the Eastern Gobi Desert of Mongolia: Usefulness of caliche for age determination. Terra Nova, 32: 246–252

Kylander-Clark A R C. 2020. Expanding the limits of laser-ablation U-Pb calcite geochronology. Geochronology, 2: 343–354

Li Q, Parrish R R, Horstwood M S A, McArthur J M. 2014. U-Pb dating of cements in Mesozoic ammonites. Chem Geol, 376: 76–83

Luo K, Zhou J X, Feng Y X, Uysal I T, Nguyen A, Zhao J X, Zhang J. 2020. *In situ* U-Pb dating of calcite from the South China antimony metallogenic belt. iScience, 23: 101575

Montano D, Gasparrini M, Gerdes A, Della Porta G, Albert R. 2021. *In-situ* U-Pb dating of Ries Crater lacustrine carbonates (Miocene, South-West Germany): Implications for continental carbonate chronostratigraphy. Earth Planet Sci Lett, 568: 117011

Moorbath S, Taylor P N, Orpen J L, Treloar P, Wilson J F. 1987. First direct radiometric dating of Archaean stromatolitic limestone. Nature, 326: 865–867

Nuriel P, Craddock J, Kylander-Clark A R C, Uysal I T, Karabacak V, Dirik R K, Hacker B R, Weinberger R. 2019. Reactivation history of the North Anatolian fault zone based on calcite age-strain analyses. Geology, 47: 465–469

Nuriel P, Weinberger R, Kylander-Clark A R C, Hacker B R, Craddock J P. 2017. The onset of the Dead Sea transform based on calcite age-strain analyses. Geology, 45: 587–590

Nuriel P, Wotzlaw J F, Ovtcharova M, Vaks A, Stremtan C, Šala M, Roberts N M W, Kylander-Clark A R C. 2021. The use of ASH-15 flowstone as a matrix-matched reference material for laser-ablation U- Pb geochronology of calcite. Geochronology, 3: 35–47

Pagel M, Bonifacie M, Schneider D A, Gautheron C, Brigaud B, Calmels D, Cros A, Saint-Bezar B, Landrein P, Sutcliffe C, Davis D, Chaduteau C. 2018. Improving paleohydrological and diagenetic reconstructions in calcite veins and breccia of a sedimentary basin by combining Δ_{47} temperature, $\delta^{18}O_{water}$ and U-Pb age. Chem Geol, 481: 1–17

Pan L, Shen A, Zhao J, Hu A, Hao Y, Liang F, Feng Y, Wang X, Jiang L. 2020. LA-ICP-MS U-Pb geochronology and clumped isotope constraints on the formation and evolution of an ancient dolomite reservoir: The Middle Permian of northwest Sichuan Basin (SW China). Sediment Geol, 407: 105728

Parrish R R, Parrish C M, Lasalle S. 2018. Vein calcite dating reveals Pyrenean orogen as cause of Paleogene deformation in southern England. J Geol Soc, 175: 425–442

Paton C, Hellstrom J, Paul B, Woodhead J, Hergt J. 2011. Iolite: Freeware for the visualisation and processing of mass spectrometric data. J Anal At Spectrom, 26: 2508–2518

Paton C, Woodhead J D, Hellstrom J C, Hergt J M, Greig A, Maas R. 2010. Improved laser ablation U-Pb zircon geochronology through robust downhole fractionation correction. Geochem Geophys Geosyst, 11: Q0AA06

Paul B, Paton C, Norris A, Woodhead J, Hellstrom J, Hergt J, Greig A. 2012. CellSpace: A module for creating spatially registered laser ablation images within the Iolite freeware environment. J Anal At Spectrom, 27: 700–706

Petrus J A, Chew D M, Leybourne M I, Kamber B S. 2017. A new approach to laser-ablation inductively-coupled-plasma mass-spectrometry (LA-ICP-MS) using the flexible map interrogation tool 'Monocle'. Chem Geol, 463: 76–93

Petrus J A, Kamber B S. 2012. VizualAge: A novel approach to laser ablation ICP-MS U-Pb geochronology data reduction. Geostand Geoanal Res, 36: 247–270

Rasbury E T, Present T M, Northrup P, Tappero R V, Lanzirotti A, Cole J M, Wooton K M, Hatton K. 2021. Tools for uranium characterization in carbonate samples: Case studies of natural U-Pb geochronology reference materials. Geochronology, 3: 103–122

Ring U, Gerdes A. 2016. Kinematics of the Alpenrhein-Bodensee graben system in the Central Alps: Oligocene/Miocene transtension due to formation of the Western Alps arc. Tectonics, 35: 1367–1391

Roberts N M W, Drost K, Horstwood M S A, Condon D J, Chew D, Drake H, Milodowski A E, McLean N M, Smye A J, Walker R J,

Haslam R, Hodson K, Imber J, Beaudoin N, Lee J K. 2020. Laser ablation inductively coupled plasma mass spectrometry (LA-ICP-MS) U-Pb carbonate geochronology: Strategies, progress, and limitations. Geochronology, 2: 33–61

Roberts N M W, Rasbury E T, Parrish R R, Smith C J, Horstwood M S A, Condon D J. 2017. A calcite reference material for LA-ICP-MS U-Pb geochronology. Geochem Geophys Geosyst, 18: 2807–2814

Roberts N M W, Walker R J. 2016. U-Pb geochronology of calcite-mineralized faults: Absolute timing of rift-related fault events on the northeast Atlantic margin. Geology, 44: 531–534

Roberts N M W, Žák J, Vacek F, Sláma J. 2021. No more blind dates with calcite: Fluid-flow vs. fault-slip along the Očkov thrust, Prague Basin. Geosci Front, 12: 101143

Rochelle-Bates N, Roberts N M W, Sharp I, Freitag U, Verwer K, Halton A, Fiordalisi E, van Dongen B E, Swart R, Ferreira C H, Dixon R, Schröder S. 2021. Geochronology of volcanically associated hydrocarbon charge in the pre-salt carbonates of the Namibe Basin, Angola. Geology, 49: 335–340

Schaltegger U, Schmitt A K, Horstwood M S A. 2015. U-Th-Pb zircon geochronology by ID-TIMS, SIMS, and laser ablation ICP-MS: Recipes, interpretations, and opportunities. Chem Geol, 402: 89–110

Shen A, Hu A, Cheng T, Liang F, Pan W, Feng Y, Zhao J. 2019. Laser ablation *in situ* U-Pb dating and its application to diagenesis-porosity evolution of carbonate reservoirs. Pet Explor Dev, 46: 1127–1140

Smith P E, Farquhar R M, Hancock R G. 1991. Direct radiometric age determination of carbonate diagenesis using U-Pb in secondary calcite. Earth Planet Sci Lett, 105: 474–491

Vermeesch P. 2018. IsoplotR: A free and open toolbox for geochronology. Geosci Front, 9: 1479–1493

Woodhead J, Hellstrom J, Maas R, Drysdale R, Zanchetta G, Devine P, Taylor E. 2006. U-Pb geochronology of speleothems by MC-ICPMS. Quat Geochronol, 1: 208–221

Woodhead J, Hellstrom J, Pickering R, Drysdale R, Paul B, Bajo P. 2012. U and Pb variability in older speleothems and strategies for their chronology. Quat Geochronol, 14: 105–113

Woodhead J, Petrus J. 2019. Exploring the advantages and limitations of *in situ* U-Pb carbonate geochronology using speleothems. Geochronology, 1: 69–84

Wu C C, Burger M, Günther D, Shen C C, Hattendorf B. 2018. Highly-sensitive open-cell LA-ICPMS approaches for the quantification of rare earth elements in natural carbonates at parts-per-billion levels. Anal Chim Acta, 1018: 54–61

Wu S, Xu C, Simon K, Xiao Y, Wang Y. 2017. Study on Ablation behaviors and Ablation Rates of a 193 nm ArF Excimer Laser System for Selected Substrates in LA-ICP-MS Analaysis (in Chinese with English Abstract). Rock Miner Anal, 36: 451–459

Wu S, Wörner G, Jochum K P, Stoll B, Simon K, Kronz A. 2019. The preparation and preliminary characterisation of three synthetic andesite reference glass materials (ARM-1, ARM-2, ARM-3) for *in situ* microanalysis. Geostand Geoanal Res, 43: 567–584

Wu S, Yang M, Yang Y, Xie L, Huang C, Wang H, Yang J. 2020a. Improved *in situ* zircon U-Pb dating at high spatial resolution (5–16 μm) by laser ablation-single collector-sector field-ICP-MS using Jet sample and X skimmer cones. Int J Mass Spectrom, 456: 116394

Wu S, Yang Y, Wang H, Huang C, Xie L, Yang J. 2020b. Characteristic performance of guard electrode in LA-SF-ICP-MS for multi-element quantification. Atom Spectro, 41: 154–161

Wu S, Yang Y, Jochum K P, Romer R L, Glodny J, Savov I P, Agostini S, De Hoog J C M, Peters S T M, Kronz A, Zhang C, Bao Z, Wang X, Li Y, Tang G, Feng L, Yu H, Li Z, Zhang L, Lin J, Zeng Y, Xu C, Wang Y, Cui Z, Deng L, Xiao J, Liu Y, Xue D, Zhang D, Jia L, Wang H, Xu L, Huang C, Xie L, Pack A, Wörner G, He M, Li C, Yuan H, Huang F, Li Q, Yang J, Li X, Wu F. 2021. Isotopic Compositions (Li-B-Si-O-Mg-Sr-Nd-Hf-Pb) and Fe^{2+} /ΣFe Ratios of Three Synthetic Andesite Glass Reference Materials (ARM-1, ARM-2, ARM-3). Geostand Geoanal Res, 45: 719–745

Yang M, Yang Y H, Wu S T, Romer R L, Che X D, Zhao Z F, Li W S, Yang J H, Wu F Y, Xie L W, Huang C, Zhang D, Zhang Y. 2020. Accurate and precise *in situ* U-Pb isotope dating of wolframite series minerals *via* LA-SF-ICP-MS. J Anal At Spectrom, 35: 2191–2203

Yang P, Wu G, Nuriel P, Nguyen A D, Chen Y, Yang S, Feng Y, Ren Z, Zhao J. 2021. *In situ* LA-ICPMS U-Pb dating and geochemical characterization of fault-zone calcite in the central Tarim Basin, northwest China: Implications for fluid circulation and fault reactivation. Chem Geol, 568: 120125

Yokoyama T, Kimura J, Mitsuguchi T, Danhara T, Hirata T, Sakata S, Iwano H, Maruyama S, Chang Q, Miyazaki T, Murakami H, Saito-Kokubu Y. 2018. U-Pb dating of calcite using LA-ICP-MS: Instrumental setup for non-matrix-matched age dating and determination of analytical areas using elemental imaging. Geochem J, 52: 531–540

Zhang L, Zhu D, Yang Y, Wang Q, Xie J, Zhao Z. 2021. U-Pb geochronology of carbonate by Laser Ablation MC-ICPMS: Method improvements and geological applications. At Spectrom, 42: 335–348

(责任编委: 刘勇胜)

SCIENCE CHINA
Earth Sciences

•RESEARCH PAPER•

https://doi.org/10.1007/s11430-021-9907-1

In situ calcite U-Pb geochronology by high-sensitivity single-collector LA-SF-ICP-MS

Shitou WU[1,2], Yueheng YANG[1,2*], Nick M. W. ROBERTS[3], Ming YANG[1,2], Hao WANG[1,2], Zhongwu LAN[1,2], Bohang XIE[1,2], Tianyi LI[4], Lei XU[1,2], Chao HUANG[1,2], Liewen XIE[1,2], Jinhui YANG[1,2] & Fuyuan WU[1,2]

[1] *State Key Laboratory of Lithospheric Evolution, Institute of Geology and Geophysics, Chinese Academy of Sciences, Beijing 100029, China;*
[2] *Innovation Academy for Earth Science, Chinese Academy of Sciences, Beijing 100029, China;*
[3] *Geochronology and Tracers Facility, British Geological Survey, Environmental Science Centre, Nottingham, NG12 5GG, UK;*
[4] *Key Laboratory of Deep Geology and Resources, Sinopec, Beijing 102206, China*

Received June 24, 2021; revised January 24, 2022; accepted February 18, 2022; published online April 27, 2022

Abstract U-Pb geochronology of calcite using laser ablation-inductively coupled plasma-mass spectrometry (LA-ICP-MS) is an emerging method, with potential applications to a vast array of geological problems. Due to the low levels of U and Pb in calcite, measurement using higher-sensitivity instruments, such as sector field (SF) ICP-MS, have advantages over more commonly used quadrupole (Q) ICP-MS instruments. Using a Thermo Element XR ICP-MS, we demonstrate that the Jet+X cone combination with the N_2 enhancement technique provides the best sensitivity for measuring U and Pb isotopes. This higher sensitivity improves the precision of calcite U-Pb isotope measurements, and permits dating at high spatial resolutions (<110 μm) and for samples containing low contents of ^{238}U (<1 μg g^{-1}) and/or ^{207}Pb (i.e., young samples <10 Ma). Using a spot size of 85 μm with a low fluence (~2.0 J cm^{-2}), the laser-induced elemental fractionation of $^{206}Pb/^{238}U$ in the NIST SRM 614, ARM-3 and WC-1 reference materials are insignificant (<2.2%). Adopting the optimized instrument parameters, we analysed four commonly-used calcite U-Pb reference materials (WC-1, Duff Brown Tank, JT, and ASH-15). The results match well with published isotope dilution data, demonstrating the reliability of our technique. ARM-3, an andesitic glass, is shown to be an appropriate reference material for both $^{207}Pb/^{206}Pb$ calibration and instrument optimization because of its moderate contents of U (~3.75 μg g^{-1}) and Pb (~12.7 μg g^{-1}). We further demonstrate that the image-guided approach using LA-ICP-MS elemental mapping is an efficient tool in obtaining robust ages.

Keywords Calcite U-Pb geochronology, SF-ICP-MS, LA-ICP-MS, Sensitivity enhancement, Jet sample cones

Citation: Wu S, Yang Y, Roberts N M W, Yang M, Wang H, Lan Z, Xie B, Li T, Xu L, Huang C, Xie L, Yang J, Wu F. 2022. *In situ* calcite U-Pb geochronology by high-sensitivity single-collector LA-SF-ICP-MS. Science China Earth Sciences, 65, https://doi.org/10.1007/s11430-021-9907-1

1. Introduction

Calcite forms in a wide variety of geological environments as both a primary and secondary mineral phase, including diagenetic, biogenic, igneous, metamorphic, and hydrothermal settings (Roberts et al., 2020). Trace amounts of uranium (U) can be incorporated in calcite during its formation, making it potentially suitable as a U-Pb chronometer (Moorbath et al., 1987; Smith et al., 1991; Jahn and Cuvellier, 1994; Woodhead et al., 2006). Calcite U-Pb geochronology has untapped potential for providing better geochronological constraints for a number of geological factors, including paleoclimate (Woodhead et al., 2006; Woodhead et al., 2012; Woodhead and Petrus, 2019; Kurumada et al., 2020), sedimentation (Drost et al., 2018; Montano et al., 2021), diagenesis (Smith et al., 1991), faulting (Roberts and Walker, 2016; Good-

* Corresponding author (email: yangyueheng@mail.iggcas.ac.cn)

fellow et al., 2017; Nuriel et al., 2017; Hansman et al., 2018; Parrish et al., 2018; Yang P et al., 2021), ore deposit formation (Burisch et al., 2017; Shen et al., 2019; Pan et al., 2020), and hydrocarbon migration (Holdsworth et al., 2019; Rochelle-Bates et al., 2021). Traditionally, calcite U-Pb dating has been carried out using isotope dilution (ID) methods and measured by thermal ionization mass spectrometry (TIMS) or multi-collector inductively coupled plasma-mass spectrometry (MC-ICP-MS) (Moorbath et al., 1987; Smith et al., 1991; Jahn and Cuvellier, 1994; Woodhead et al., 2006). However, this technique has not been used extensively, owing in part to the time-intensive nature of dissolution and column chemistry that necessitates sample preparation within a specialised clean laboratory, and to the poor spatial resolution that leads to an averaging of the isotopic zonation within a single aliquot.

Since the first use of laser ablation (LA)-ICP-MS dating of diagenetic calcite cement in fossils (Li et al., 2014), this technique has successfully been used to date calcite in a growing number of laboratories (Coogan et al., 2016; Ring and Gerdes, 2016; Goodfellow et al., 2017; Drost et al., 2018; Pagel et al., 2018; Parrish et al., 2018; Yokoyama et al., 2018; Woodhead and Petrus, 2019; Cheng et al., 2020; Guillong et al., 2020; Kurumada et al., 2020; Luo et al., 2020; Pan et al., 2020; Hoareau et al., 2021; Yang P et al., 2021). Compared with ID-TIMS, LA-ICP-MS has the advantages of high spatial resolution and the ability to rapidly generate large datasets with significant variations in U-Pb ratios. However, calcite is generally characterized by low U contents. For example, Roberts et al. (2020) reported the U and Pb content data of carbonate minerals generated in their laboratory over several years, which have median U and Pb_{total} contents of 1.9 and 0.003 μg g^{-1}. Therefore, high sensitivity ICP-MS instruments (e.g., sector field ICP-MS: Thermo Element 2/XR, Nu Plasma and Nu Attom) have been used in numerous laboratories (Li et al., 2014; Roberts et al., 2017; Hansman et al., 2018; Guillong et al., 2020; Hoareau et al., 2021). The high sensitivity of Jet sample (Jet) and X version skimmer (X) cones that are compatible with the Thermal Element XR could potentially enhance sensitivity (and possibly thereby analytical precision) of this sector field single collector instrument (Hu et al., 2012; He et al., 2018; Wu et al., 2018; Guillong et al., 2020; Wu et al., 2020a; Yang et al., 2020; Yang Y et al., 2021). Yokoyama et al. (2018) reported the use of Jet and X cones on the Neptune Plus MC-ICP-MS for calcite U-Pb geochronology. However, the high sensitivity capability of the Element XR has not been fully explored for calcite U-Pb geochronology.

In this study, we investigate the sensitivity of three cone combinations (S+H, Jet+H, and Jet+X) with and without the addition of nitrogen on calcite U-Pb geochronology. The laser-induced elemental fractionations of $^{206}Pb/^{238}U$ in different reference materials (RMs) were evaluated. Using a set of optimized instrument parameters, we analysed four common-used calcite U-Pb RMs systematically (WC-1, Duff Brown Tank, JT, and ASH-15). The accurate calibration of $^{207}Pb/^{206}Pb$ for calcite based on the newly developed ARM-3 glass was verified. We also demonstrate the image-guided approach using LA-ICP-MS elemental mapping on an unknown sample, and demonstrate that it can generate precise analyse with only a limited increase in analytical time and effort.

2. Materials and methods

2.1 Samples

A total of six samples were used in this study, two glasses and four calcite U-Pb RMs, which have been well characterized in previous studies (Jochum et al., 2011; Roberts et al., 2017; Wu et al., 2019, 2021; Guillong et al., 2020). Detailed information is given in Table 1. These RMs are used for the validation of our technique.

2.1.1 NIST SRM 614

This is a synthetic soda lime glass with trace elements at levels of ~0.8 to 3.0 μg g^{-1} (Jochum et al., 2011). This reference glass is commonly used for the calibration of $^{207}Pb/$

Table 1 Silicate glass Pb-Pb and calcite U-Pb reference materials used in this study

Name	Matrix	Locations	Age (Ma)	Uncertainty (Ma)	U contents (μg g^{-1})	Characterization technique	Reference
NIST SRM 614	Synthetic soda lime glass	–	–	–	0.823	ICP-MS	Jochum et al., 2011
ARM-3	Synthetic andesite glass	–	–	–	3.75	ICP-MS	Wu et al., 2019
WC-1	Marine calcite	Delaware Basin of West Texas, USA	254	6.4	~5	ID-TIMS	Roberts et al., 2017
Duff Brown	Limestone	Coconino Plateau, northwest of Williams, Arizona, USA	64.04	0.67	5–20	ID-MC-ICP-MS	Hill et al., 2016
JT-1	Calcite	Northern Swiss Molasse Basin, Switzerland	13.797	0.031	~0.5	ID-TIMS	Guillong et al., 2020
ASH-15D	Calcite	Central Negev Desert, southern Israel	2.965	0.011	2–5	ID-TIMS	Nuriel et al., 2021

^{206}Pb (and ^{208}Pb/^{206}Pb) ratios of calcite across all laboratories. Although NIST SRM 614 has a different matrix than calcite, there is currently no evidence to suggest that the Pb-Pb isotope ratios fractionate across different matrices (Guillong et al., 2020; Roberts et al., 2020).

2.1.2 ARM-3

This newly developed andesitic glass RM has trace-element contents of ~5 μg g^{-1}. The 54 major and trace elements were characterized via different techniques (Wu et al., 2019). Recently, multiple isotope ratios (Li, B, Si, O, Mg, Sr, Nd, Hf and Pb) were characterized using a range of techniques (Wu et al., 2021). The capability of ARM-3 for calibration of the ^{207}Pb/^{206}Pb ratio of calcite is evaluated in this study.

2.1.3 WC-1

Walnut Canyon-1 (WC-1) is taken from a ~1 kg hand sample of marine calcite cement from a fault-related discordant neptunian dyke in a Permian (Capitanian) reef complex exposed in the Guadalupe Mountains on the western side of the Delaware Basin, West Texas, USA. ID-TIMS data from the sample yield an age of 254.4±6.4 Ma (2σ) and it contains 85–98% radiogenic lead (Roberts et al., 2017). WC-1 contains ~5 μg g^{-1} U. WC-1 is currently the only well-characterized RM used in most laboratories undertaking calcite U-Pb geochronology.

2.1.4 Duff Brown Tank

This sample was collected at Duff Brown Tank, where lenses of coarse-grained arkose sandstone within clay-rich siltstone are interbedded with the Long Point limestone. The Long Point limestone is a white to light-gray lacustrine unit located on the Coconino Plateau, ~60 km northwest of Williams, Arizona, USA. ID-MC-ICP-MS analyses of the sample yield an age of 64.04±0.67 Ma (Hill et al., 2016). The Duff Brown Tank contains 5–20 μg g^{-1} U.

2.1.5 JT

This sample is vein calcite from a deep borehole in the northern Swiss Molasse Basin, where it is hosted by micritic limestone of the Middle Triassic Mushelkalk Group. The sample was obtained from part of a dense network of calcite veins associated with a thrust fault that branches off from the basal decollement of the Jura fold and thrust belt. JT has been characterized by ID-TIMS, yielding an age of 13.797±0.031 Ma (Guillong et al., 2020). JT contains ~0.5 μg g^{-1} U.

2.1.6 ASH-15

ASH-15 is a flowstone found in Ashalim Cave in the central Negev Desert, southern Israel. The cave entrance is 414 m above sea level and 67 km SE of the coast of the Mediterranean Sea. The most recent ID-TIMS analyses of ASH-15 yielded an age (uncorrected for disequilibrium) of 2.965 ±0.011 Ma (Nuriel et al., 2021). This calcite is used in several laboratories, but it requires more-sensitive ICP-MS instrumentation due to its low contents of radiogenic Pb. The U contents of ASH-15 range from 2 to 5 μg g^{-1}.

2.2 LA-Q-ICP-MS element-image analysis

LA-quadrupole (Q)-ICP-MS elemental analyses were carried out at the Institute of Geology and Geophysics, Chinese Academy of Sciences, Beijing, China (IGGCAS). The samples were mounted into one- or half-inch (2.5 or 1.25 cm-diameter) epoxy mounts then polished. The mounts were assembled in the HelEx-II ablation cell for screening for ^{206}Pb, ^{207}Pb, ^{208}Pb, ^{232}Th and ^{238}U isotopes and trace elements (^{24}Mg, ^{29}Si, ^{43}Ca, ^{55}Mn, ^{57}Fe, ^{69}Ga, ^{85}Rb, ^{88}Sr, ^{90}Zr, ^{137}Ba, ^{139}La, ^{140}Ce, ^{141}Pr, ^{146}Nd, ^{147}Sm, ^{153}Eu, ^{158}Gd, ^{159}Tb, ^{163}Dy, ^{165}Ho, ^{166}Er, ^{169}Tm, ^{173}Yb, and ^{175}Lu) using the Photo Machine Analyte G2 193 nm ultraviolet (UV) ArF-Excimer laser ablation system (Teledyne CETAC, Omaha, USA) coupled with an Agilent 7500a Q-ICP-MS (Agilent Technologies, Santa Clara , USA). The laser repetition rate and fluence were set to 15 Hz and 2.0 J cm^{-2}. The laser spot size used was 50 μm and the line scan speed was 40–50 μm s^{-1}. The NIST SRM 614 and ARM-3 RMs were used to quantify elemental contents, assuming the values of Jochum et al. (2011) and Wu et al. (2019), respectively. Trace element data were reduced using Iolite software with the "Trace_Element" DRS and the "semi quantitative" standardization method. 2D elemental image were generated using Iolite software v4 (Paul et al., 2012; Petrus et al., 2017). The detailed analytical procedures are given in Table 2.

2.3 LA-SF-ICP-MS U-Pb analysis

I*n situ* calcite U-Pb dating was carried out using LA-SF-ICP-MS at the IGGCAS using a Photo Machine Analyst G2 laser ablation system (Teledyne CETAC, Omaha, USA) coupled to an Element XR (Thermo Fisher Scientific, Bremen, Germany). The Element XR instrument is equipped with a high-capacity vacuum pump (OnTool Booster 150, Asslar, Germany), with which the high-performance Jet sample cone can be used. A small amount of nitrogen added to the Ar sample gas could lead to enhanced sensitivity and reduced oxide production rates (Hu et al., 2008). Four types of cone were used in this study, including a standard sample cone (S), an H version skimmer cone (H), a Jet sample cone (Jet), and an X-version skimmer cone (X). Three cone combinations (S +H, Jet+H, and Jet+X) with and without the addition of nitrogen were investigated to test the sensitivity of U and Pb isotope measurements. The guard electrode was used in all experiments to improve sensitivity (Wu et al., 2020b). A T-junction was used to add N_2 to the Ar sample gas flow after the ablation cell using an MKS GE50 mass flow controller

Table 2 Instrumental parameters of LA-(Q, SF)-ICP-MS for elemental imaging and U-Pb geochronology

Parameters	Elemental mapping	U-Pb geochronology
Laser ablation system		
Make, Model & type	Photon Machines Analyte G2	Photon Machines Analyte G2
Ablation cell & volume	HelEx ablation cell	HelEx ablation cell
Laser wavelength	193 nm	193 nm
Pulse width	~5 ns	~5 ns
Energy density/fluence	~ 3 cm^{-2}	~ 2 J cm^{-2}
Repetition rate	15 Hz, 20 Hz	8 Hz
Spot size	50 μm	85. 110 μm
Sampling mode/pattern	Line scaoning with a speed of 40–50 m s^{-1}	Single hole drilling, two cleaning pulse
Ablation gas flow (He)	~0.75 L min^{-1}	~0.75 L min^{-1}
Ablation duration	variable	30 seconds
ICP-MS		
Make, model & type	Agilent 7500a	Thermo Fisher Scientific Element XR
RF Power	1350 W	1320 W
Guard electrode (Pt)	Disconnected	Connected
Sample cone	nickel AT1001-Ni	nickel standard cone, Jet sample cone
Skimmer cone	nickel AT1002-Ni	nickel "H" skimmer cone, X-version skimmer cone
Coolant gas flow (Ar)	15.00 L min^{-1}	15.00 L min^{-1}
Auxiliary gas flow (Ar)	0.80 L min^{-1}	0.80 L min^{-1}
Carrier gas flow (Ar)	1.15 L min^{-1}	0.95 L min^{-1}
Enhancement gas flow (N_2)	No	4 mL min^{-1} for S+H; 6 mL min^{-1} for Jet+H, Jet+X
Scan mode	Peak jump	E-scan
Isotopes measured (m/z)+ sample time (ms)	^{24}Mg (6), ^{29}Si(6), ^{43}Ca(6), ^{55}Mn(6), ^{57}Fe(6), ^{69}Ga(6), ^{85}Rb(6), ^{88}Sr(6), ^{90}Zr(6), ^{137}Ba(6), ^{139}La(6), ^{140}Ce(6), ^{141}Pr(6), ^{146}Nd(6), ^{147}Sm(6), ^{153}Eu(6), ^{158}Gd(6), ^{159}Tb(6), ^{163}Dy(6), ^{165}Ho(6), ^{166}Er(6), ^{169}Tm(6), ^{173}Yb(6), ^{175}Lu(6), ^{206}Pb (15), ^{207}Pb (25) , ^{208}Pb (2), ^{232}Th (2), ^{238}U (10)	^{202}Hg(2), ^{204}Pb(2), ^{206}Pb(15), ^{207}Pb(25) , ^{208}Pb(2), ^{232}Th(2), ^{238}U(10)
Mass window	–	20%
Sample per peak	–	20
Detection system	Single SEM in double mode, Counting and Analog	Single SEM detector in triple mode, Counting, Analog and Faraday
Resolution (M/ΔM)	~300	~300
Total integration time per reading	0.35 s	0.27 s

(Coastal instruments, Burgaw, NC, USA).

Data were acquired in fully-automated mode in sequences of 60 to 80 spot analyses. Each spot analysis consists of 8 s of background acquisition followed by 25 s of sample ablation and 30 s washout. During data acquisition, signal intensities of ^{202}Hg, ^{204}(Hg+Pb), ^{206}Pb, ^{207}Pb, ^{208}Pb, ^{232}Th, and ^{238}U were measured in peak-jumping mode with a total intergration time of 0.27 s, resulting in 130 mass scans. The isotopic abundances were collected using triple mode with automatical switching between counting, analog and Faraday cup. These different modes were calibrated prior to the analysis of unknowns using the $^{36}Ar^{+}$ peak. Two analyses of soda-lime glass NIST SRM 614, two analyses of andesitic glass ARM-3, and three analyses of the calcite RM WC-1 were used to bracket every ten analyses of unknown samples. For each of the studied samples, 30–40 spot analyses were collected; the Duff Brown Tank, JT and ASH-15 RMs were treated as unknowns. Detailed information on the instrumentation is given in Table 2.

The methods of data reduction largely follow those of Roberts et al. (2017), Ring and Gerdes (2016), Hansman et al. (2018), Nuriel et al. (2021), and are described here in brief. The raw data (time-resolved intensities) from the spectrometer were loaded into the Iolite 3.7 data reduction software (Paton et al., 2011). For the first step, NIST SRM 614 was used as the RM to correct for instrument drift and to

calculate the isotopic ratios of $^{207}Pb/^{206}Pb$ and $^{206}Pb/^{238}U$ and their uncertainties. This was accomplished using the VisualAge data reduction scheme (Petrus and Kamber, 2012). Any laser induced elemental fractionations of WC-1 and other samples were corrected using the fractionation profile derived from analysis of RM NIST SRM 614, using the approach described by Paton et al. (2010). After initial correction, a matrix-matched sample of WC-1 was used to correct for matrix-induced mass bias of $^{238}U/^{206}Pb$ ratios between NIST SRM 614 and calcite using Microsoft Excel. This two-step calibration is illustrated in Figure 1. The additional offset factor varied during the different analytical sessions (see details in section 3.6). The data were plotted and evaluated using IsoplotR (Vermeesch, 2018).

3. Results and discussion

3.1 Laser induced elemental fractionation

Laser induced elemental fractionation (LIEF) is defined as changes in Pb/U ratios during excavation of laser craters (Jeffries et al., 1998, 2003) and is one of the main factors affecting the precision of measured Pb/U ratios. It is important to note that the LIEFs can vary among different laboratories, or through using different laser parameters in a single laboratory (Paton et al., 2010). It is always preferable to correct for any LIEF effects using calibration of known RMs (Woodhead and Petrus, 2019). We evaluated the LIEFs of NIST SRM 614, ARM-3, and WC-1 under a specific set of instrumental conditions. Figure 2 plots the $^{206}Pb/^{238}U$ LIEF patterns of NIST SRM 614, ARM-3, and WC-1 as a function of ablation time; the average of 12–18 individual replicate measurements (red curves). The linear regression of LIEF based on the average of individual measurements (black lines).

Figure 2 illustrates that the effects of LIEF are insignificant for analyses of the NIST SRM 614, ARM-3, and WC-1 RMs using laser spot size of 85 μm, energy density of ~2.0 J cm^{-2}, and laser frequency of 8 Hz. The number-% in Figure 2 was the relative increment of signal intensity after the laser ablation. A value of 0% means no LIEF was observed during ablation. For the NIST SRM 614, ARM-3, and WC-1 RMs, low values of 0.7%, –2.2%, and –1.1%, respectively, are insignificant. Low degrees of LIEFs are explained by the large laser spot sizes (85 μm) and the shallow crater depth (20–30 μm), resulting in a small depth/diameter ratio. The crater depth is estimated based on the calculation of 200 laser pulses multiplied by ablation rates (0.10–0.15 μm pulse^{-1}, estimated from a previous study of Wu et al. (2017)). Several individual measurements of WC-1 show scatter with elevated Pb/U ratios, which are probably related to the high common-Pb regions. The uncertainty on the normalization of Pb/U ratios derived from LIEF alone is <2.2%. This is typically within analytical uncertainty of individual analyses, which are propagated from both statistical analysis and the natural heterogeneity of the material. We note that the patterns of LIEFs observed here may differ from those in other laboratories because of the different instrument types and laser parameters used, and results will also vary as function of the geometry of the laser pit, particularly the depth/diameter ratio.

3.2 Sensitivity of different cone combinations

Figure 3 plots the sensitivity of ^{238}U and ^{206}Pb in three cone combinations (S+H, Jet+H and Jet+X) with and without the addition of nitrogen. Analyses used a laser spot size of 85 μm with an energy density of ~2 J cm^{-2}, and a laser frequency of 8 Hz. Notably, the sensitivity defined here is the best sensitivity under tuned instrument conditions of $ThO^+/Th^+ < 1.0\%$

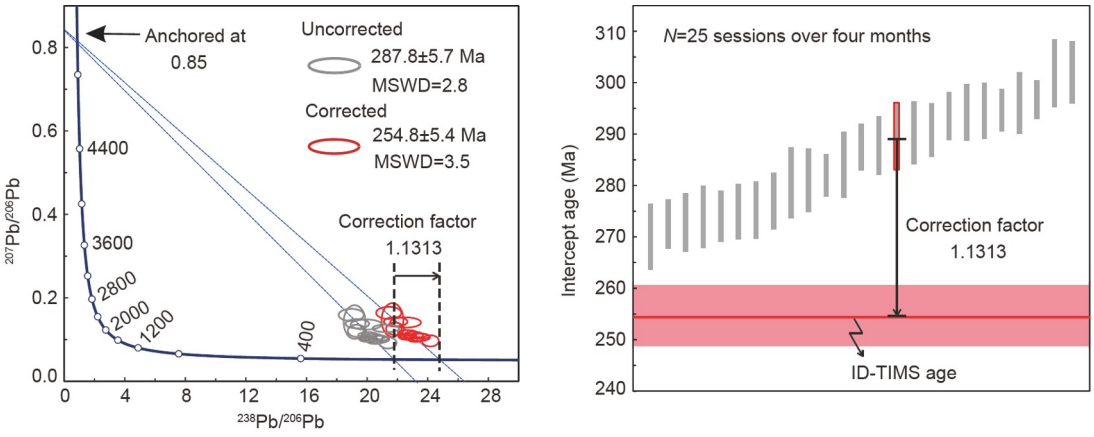

Figure 1 Plots illustrating the two-step calibration strategy for calcite U-Pb geochronology using Tera-Wasserburg plots. Uncorrected ages were derived directly from the Iolite software package using NIST SRM 614 as the primary RM for $^{207}Pb/^{206}Pb$ and $^{238}U/^{206}Pb$ ratio correction. A total of 25 sessions over 4 months yielded correction factors ranging from 1.063 to 1.189. Correction factors were calculated as the bias between the NIST SRM 614 as the primary RM and the ID-TIMS values.

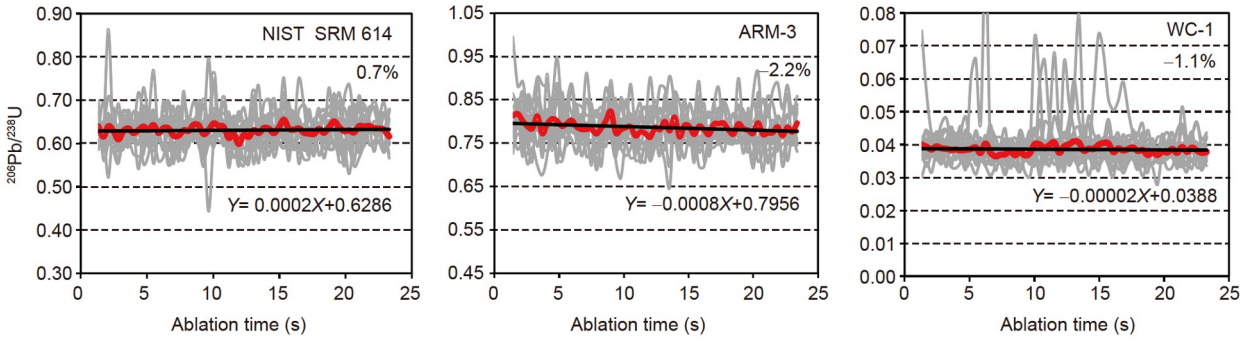

Figure 2 LIEF $^{206}Pb/^{238}U$ patterns for NIST SRM 614, ARM-3, WC-1. The laser spot size was 85 μm with an energy density of ~2.0 J cm^{-2} and a laser frequency of 8 Hz. The LIEF patterns were simulated using a linear relationship. The percentage value is the calculated relative increment after laser ablation. A value of 0% means no observed LIEF during ablation. The results indicate that the LIEF for the three RMs is insignificant (<2.2%).

and Th^+/U^+ ratio in the range of 0.9 to 1.1. In all three cone combinations, the addition of nitrogen provides better sensitivity than that of without the addition of nitrogen by a factor of ~3 for S+H, ~1.5 for Jet+H, and ~10 for Jet+X. We observed a very high oxide production rate (ThO^+/Th^+ >30%) for the Jet+X without the addition of nitrogen, but this was significantly reduced to <1.0% with the addition of nitrogen. Thus, the enhanced sensitivity of the addition of nitrogen is partially attributable to a reduced oxide production rate (Wu et al., 2020a). The sensitivity of the three cone combinations are Jet+X>Jet+H>S+H, excluding the Jet+X under the condition of without nitrogen. The low sensitivity of Jet+X cones without the addition of nitrogen is attributed mainly to extremely high oxide production, which is probably related to the design of the X version cones.

Compared with the S cones, the Jet cone has a large orifice. The H and X cones both have orifices of 0.8 mm, but the H cone has a cylindrical entrance and a trumpet-shaped exit, whereas an X cone is completely trumpet-shaped (Bouman et al., 2009). Thus, the Jet+X cone combination provides more space for ion beams to enter the orifice than other cone combinations. We attribute this feature to the improved sensitivity for Jet+X cone combinations. As shown in Figure 3, the sensitivity of the Jet+X cones with the addition of nitrogen is about 350,000 cps $(\mu g\ g^{-1})^{-1}$ for ^{238}U at 85 μm laser spot size, ~2.0 J cm^{-2} laser energy, and 8 Hz frequency at a sensitivity (defined as #ions detected/#atoms measured) of 0.76% (Schaltegger et al., 2015).

For comparison with other instrumentation, we recalculated the results of Hansman et al. (2018) and Ring and Gerdes (2016) using a Thermo Element 2 instrument (S+H cones with the addition of nitrogen) to yield sensitivity values of 0.13–0.17%. Thus, our data are compatible with a three- to four-fold increase in the sensitivity of the Element XR with Jet+X cones installed. This sensitivity is at least ten times greater than that of Q-ICP-MS. Given the low U and Pb contents of many calcite grains, the common compositional zonation at the micron level, and the common occurrence of inclusions, it is preferable that analysts use as small

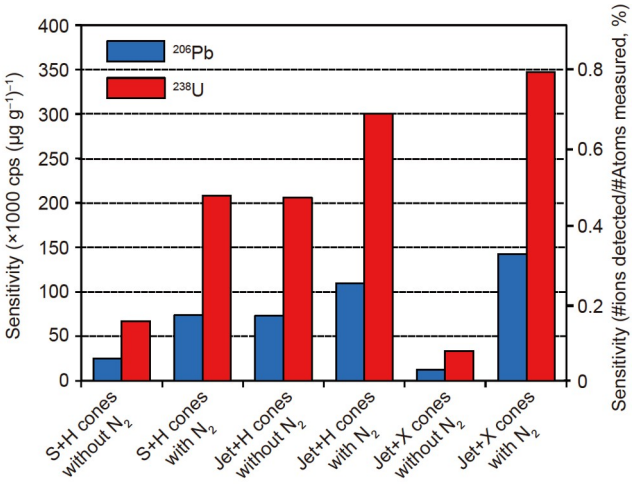

Figure 3 Signal sensitivities of ^{206}Pb and ^{238}U in three cone combinations (S+H, Jet+H and Jet+X) with and without the addition of nitrogen. Signal data were collected using line-scanning mode with a spot size is 85 μm, an energy density of ~2.0 J cm^{-2}, and a laser frequency of 8 Hz. The ablated sample is NIST SRM 612. The Jet+X cone combination with the addition of nitrogen provides the best intensities for ^{206}Pb and ^{238}U isotopes. The sensitivity is given as cps $(\mu g\ g^{-1})^{-1}$ and by the #number of ions detected/#number of atoms measured (Schaltegger et al., 2015).

a spot size as possible, while maintaining good precision. The increased sensitivity shown here means that small spot sizes are applicable, potentially opening up further applications of calcite geochronology, for example to investigate fine-scale pore cements.

3.3 Improvements using Jet sample and X skimmer cones with N_2 enhancement technique

The JT calcite RM has low U contents (~0.5 μg g^{-1}) and is young (ca. ~14 Ma); so it was selected to demonstrate the advantages of the enhanced sensitivity of the instrument used in this study. Figure 4a–4c compares the dating results for the JT sample using three cone combinations (S+H without the addition of nitrogen, Jet+H without the addition of nitrogen, and Jet+X with the addition of nitrogen). The lower intercept

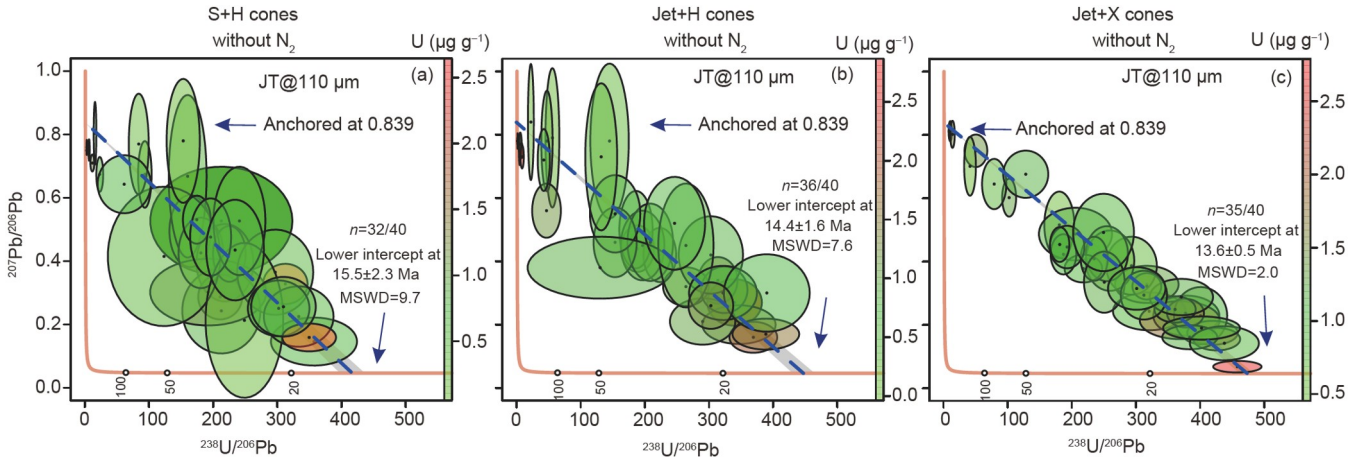

Figure 4 Tera-Wasserburg diagrams of sample JT using three instrument conditions (S+H cones without the addition of nitrogen, Jet+H cones without the addition of nitrogen and Jet+X cones with the addition of nitrogen). Lower intercept ages were calculated using an anchored ^{207}Pb/^{206}Pb value of 0.839 (Guillong et al., 2020). The accuracy and precision are significantly improved using high-sensitivity Jet+X cones with the addition of nitrogen. Several data are identified as outliers. In *n*=*a*/*b*, "*a*" indicate the numbers used for plotting and "*b*" represents the total numbers of analyses. Data were plotted and evaluated using IsoplotR (Vermeesch, 2018).

ages of 15.5±2.3, 14.4±1.6, and 13.6±0.5 Ma were obtained using S+H without the addition of nitrogen, Jet+H without the addition of nitrogen, and Jet+X with the addition of nitrogen, respectively. Although these ages are in broad agreement with the ID-TIMS age (13.797±0.031 Ma; Guillong et al., 2020), both the data-point and the final ages using the Jet+X cones with the addition of nitrogen have greater precision. The internal precision that is the precision of individual spot analysis (2SE), is improved with the use of the Jet+X cones with the addition of nitrogen, which is a result of the better counting statistics facilitated by the enhanced sensitivity.

3.4 Correction of ^{207}Pb/^{206}Pb using NIST SRM 614 and ARM-3

Figure 5a plots the precisions of measurements of ^{207}Pb/^{206}Pb in NIST SRM 614 and ARM-3 along with the signal intensity of ^{207}Pb. Compared with NIST SRM 614, ARM-3 contains higher contents of Pb (12.7 μg g^{-1} vs. 2.32 μg g^{-1}), thereby providing better counting statistics for the calibration of ^{207}Pb/^{206}Pb. The ^{207}Pb/^{206}Pb results of WC-1, Duff Brown Tank, JT and ASH-15 are in agreement for the calibration using NIST SRM 614 and ARM-3 (Figure 5b), indicating a negligible matrix-induced effect on ^{207}Pb/^{206}Pb ratios for NIST SRM 614 and ARM-3. These results indicate that ARM-3 is a potential RM for ^{207}Pb/^{206}Pb corrections. ARM-3 contains moderate U (~3.75 μg g^{-1}), similar to that of the calcite RM WC-1. Given the sensitivity of the Element XR used here, this should provide a signal intensity of ^{238}U in ARM-3 of >1 million cps. Thus, ARM-3 is a suitable choice for both instrument optimization and calculating the ^{207}Pb/^{206}Pb correction in calcite U-Pb geochronology. The ^{206}Pb/

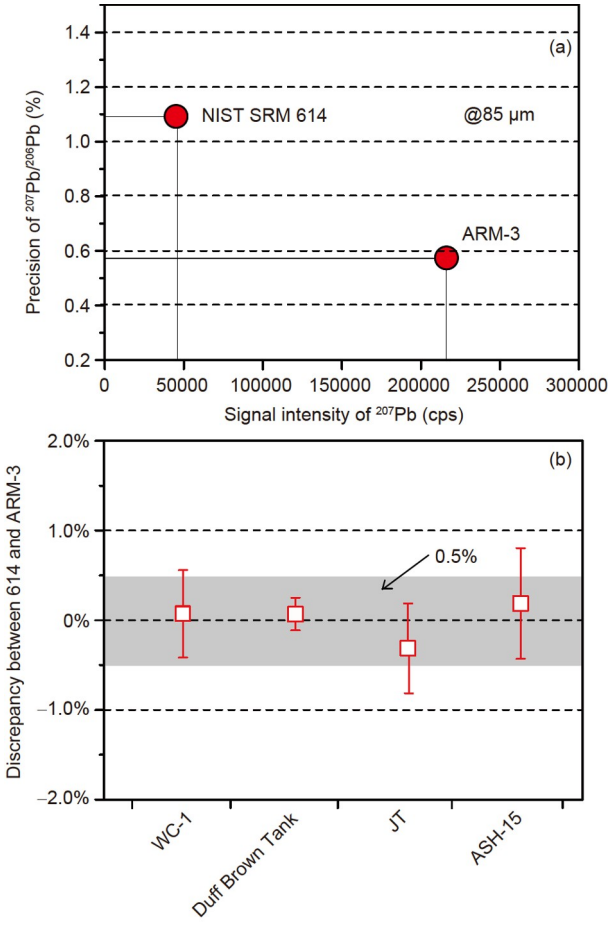

Figure 5 (a) Plot illustrating the analytical precision of ^{207}Pb/^{206}Pb ratios in NIST SRM 614 and ARM-3 along with the signal intensity of ^{207}Pb. (b) Plot comparing the measured ^{207}Pb/^{206}Pb ratios of WC-1, Duff Brown Tank, JT, and ASH-15 calibrated using NIST SRM 614 and ARM-3. The discrepancy is calculated as (unity minus results from 614/results from ARM-3) ×100. The data indicate the negligible matrix-induced ^{207}Pb/^{206}Pb bias between RMs NIST SRM 614 and ARM-3.

^{238}U ratio of ARM-3 has not yet been determined. However, ARM-3 can be utilized as an additional Pb/U RM after further characterization of the $^{206}Pb/^{238}U$ ratio in the future.

3.5 LA elemental mapping

Trace-element contents in calcite can be variable at the μm-scale (Roberts et al., 2020; Rasbury et al., 2021). 2D elemental images thus provide important information for understanding the petrogenesis and alteration of calcite, as well as for locating the zones of highest U content that are preferable for U-Pb geochronology (Roberts et al., 2020). Although WC-1 has been mapped for its trace-element contents (Roberts et al., 2017), individual sample grains may be compositionally heterogeneous. Guillong et al. (2020) reported that the dark (in reflected light) part of their WC-1 yield results that were in agreement with the recommended age (254.4±6.4 Ma; Roberts et al., 2017), whereas the brighter vein-like part gave more scattered and younger ages. Therefore, it is necessary to evaluate the compositional variability of any RMs used for primary normalization, as all calcite has the possibility for heterogeneous elemental and isotopic compositions. The Duff Brown Tank sample has been used as a case study for image-based dating (Drost et al., 2018). Here we provide the results of compositional mapping of WC-1, Duff Brown Tank, and JT.

As shown in Figure 6, the trace-element compositions of the three RMs appear to be distributed heterogeneously at the μm-scale. For WC-1 and Duff Brow Tank, U contents are positively correlated with La, but not with Sr or Mg. The Sr content of sample WC-1 is much higher than that of Duff Brown Tank, indicating WC-1 as a potential RM for *in situ* Sr isotope analysis (Rasbury et al., 2021). In sample JT, the trace elements are clearly distributed in two separate areas. The right-hand part is country rock with high contents of Mg, Sr, La and U, whereas the left-hand part is the calcite vein with a recommended age of 13.797±0.031 Ma. As a result, we recommend mapping trace elements individually for calcite RMs to provide more robust information on sample quality.

3.6 U-Pb dating results for WC-1, Duff Brown Tank, JT, and ASH-15

3.6.1 WC-1

As the WC-1 sample was used to calibrate Pb/U ratios, the age results cannot be used to evaluate the accuracy of the technique. A total of 25 analytical sequences were carried out for sample WC-1 over four months; the results are summarized in Figure 1. The laser spot size and frequency are kept consistent in all 25 analytical sequences, but with different cone combinations. The correction factor varied from 1.063 to 1.189, owing mainly due to the daily settings of the instrument. However, the matrix effect between NIST SRM 614 and calcite can be effectively corrected using the derived correction factor.

3.6.2 Duff Brown Tank

We analysed the Duff Brown Tank sample over four sessions (three using a laser beam diameter of 85 μm and one using 50 μm; Figure 7). The data (Supplement Table S1, https://link.springer.com) are plotted in Tera-Wasserburg diagrams with both unconstrained and constrained discordia lines; for the latter, the $^{207}Pb/^{206}Pb$ ratio was anchored at 0.738 (Hill et al., 2016). This sample contains 18.6–86.7% common Pb. The precision of individual analyses is mostly < 3.0% (2σ) for $^{238}U/^{206}Pb$ and < 4.0% (2σ) for $^{207}Pb/^{206}Pb$. The mean values of the U contents obtained in the four sessions are 15.1±9.4 μg g^{-1}. For the unconstrained discordia results, the four sessions yielded lower intercept ages of 62.9±1.7, 62.7 ±1.5, 64.4±1.1, and 63.8±1.7 Ma, respectively, which are slightly younger than the reported ID-TIMS age (64.04±0.67 Ma), but in agreement within measurement uncertainty. The $^{207}Pb/^{206}Pb$ ratio (0.662–0.698) on the Y-intercept is significantly lower than the reported value (0.738±0.01; Hill et al., 2016), a phenomenon observed in all four analytical sessions (Figure 7).

For the constrained discordia, four sessions yielded ages of 65.5±0.6, 66.7±0.7, 66.6±0.6, and 65.8±0.5 Ma, respectively, which are sytematically older than the reported ID-TIMS age (64.04±0.67 Ma), but still within 3.5% of the LA-ICP-MS measurement uncertainty. Such systematically biased $^{238}U/^{206}Pb$ and $^{207}Pb/^{206}Pb$ ratios would shift the discordia lines in a parallel direction. This means that, if the unconstrained lines were forced to $^{207}Pb/^{206}Pb$ values of 0.738, the lower intercept age would be even younger, indicating the lower Y-intercept $^{207}Pb/^{206}Pb$ ratio is not an artefact of either measurement or calibration. To verify this, we carried out one additional session using LA-MC-ICP-MS (a Resolution M50 laser coupled to a Neptune Plus MC-ICP-MS) from an independent laboratory (Zhang et al., 2021). The results (Supplement Figure S1) are similar to our LA-SF-ICP-MS data, perhaps indicating heterogeneity in the initial $^{207}Pb/^{206}Pb$ ratio of the Duff Brown Tank RM. It should be emphasized that the spatial resolution may be reduced to 50 μm or less, owing to the high U contents.

3.6.3 JT

This JT sample was measured over two sessions. The data are summarized in Supplement Table S2 and plotted in Figure 8. The separate calcite vein and country rock parts were measured in sessions 1 and 2, respectively. Session 1 yielded an intercept age of 13.76±0.43 Ma, which is in agreement with the ID-TIMS age (13.797±0.031 Ma) reported by Guillong et al. (2020). Session 2 yielded an intercept age of 151.5±13.7 Ma. To our knowledge, this is the first age constraint on the JT country rock. As shown in Figure 8, the U content in the

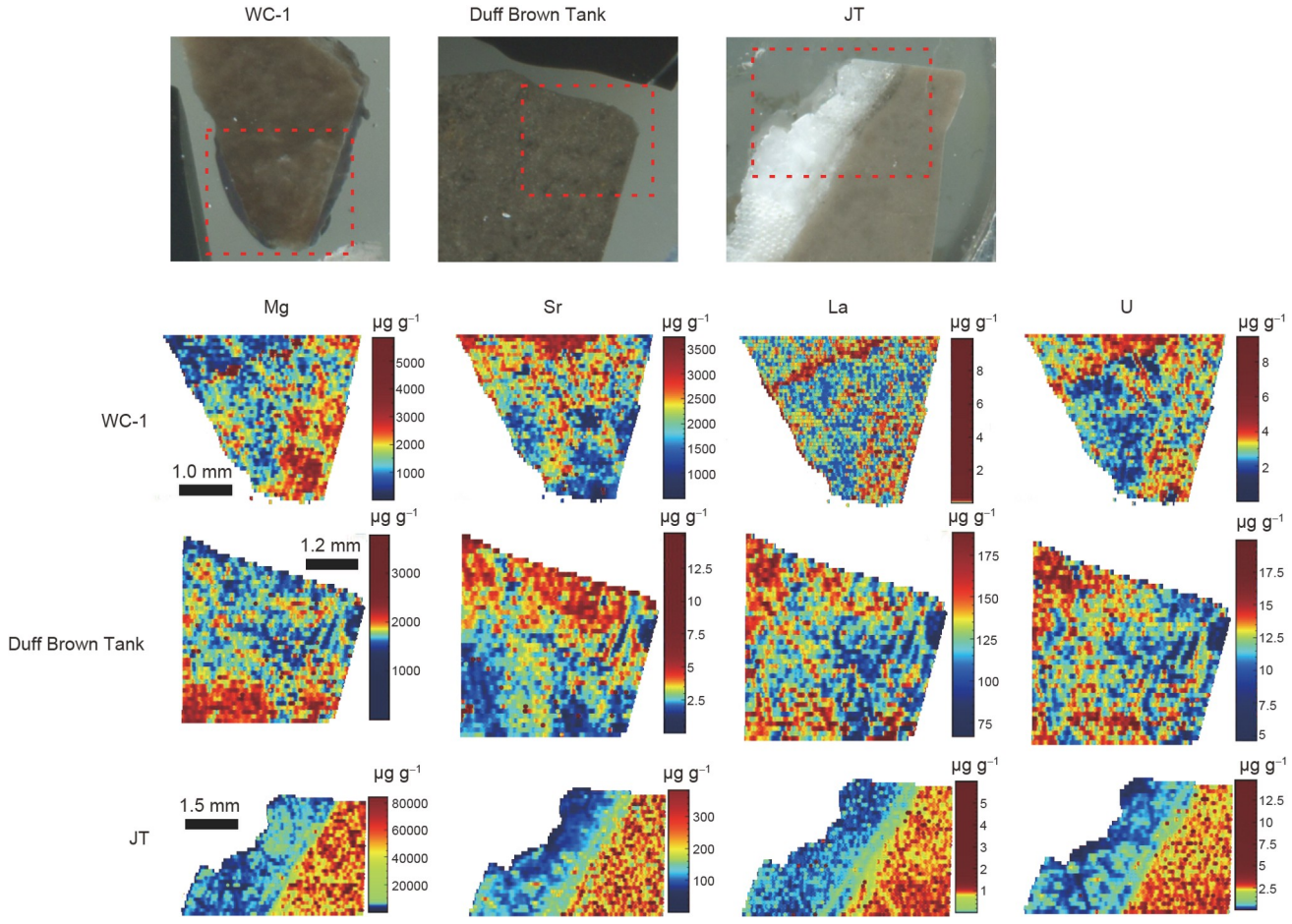

Figure 6 Elemental maps showing contents (in μg g^{-1}) of Mg, Sr, La and U in WC-1, Duff Brown Tank, and JT. The images illustrate a heterogeneous distribution of these elements at a micron scale. The corresponding pictures in optical reflected light are provided.

calcite vein is 0.56±1.00 μg g^{-1}, and in the country rock is 0.88 ±0.34 μg g^{-1}. A common Pb component is dominant in the country rock, whereas it is more variable in the calcite vein.

3.6.4 ASH-15

The data for the two analytical sessions for the ASH-15 sample are summarized in Supplement Table S3, and plotted in Figure 9. Session 1 yielded an intercept ages of 2.947 ±0.063 Ma (anchored in 0.832) and 2.987±0.080 Ma (unconstrained, $^{207}Pb/^{206}Pb_0$: 0.860±0.035). Both ages overlap with the accepted ID-TIMS age within analytical uncertainty (2.965±0.011 Ma; Nuriel et al., 2021). Session 2 yielded an intercept age of 3.037±0.067 Ma (anchored in 0.832) and 3.044±0.075 Ma (unconstrained, $^{207}Pb/^{206}Pb_0$: 0.840±0.034). Two ages have a positive offset of ~2.7% than the accepted ID-TIMS age. This offset is within the expected uncertainty associated with matrix-matching (2–3%) as demonstrated by Guillong et al. (2020) and Nuriel et al. (2019). The U content of the ASH-15 sample obtained from two sessions is 1.62± 0.91 μg g^{-1}. This sample was slightly easier to measure with JT because of the high U contents, despite the young age. The background intensity of ^{207}Pb is ~17.6 cps on our instrument, whereas the ^{207}Pb signal intensities of WC-1 (85 μm), ASH-1(110 μm) and JT (110 μm) are 1295–3388 cps, 28–1871 cps, and 136–591 cps, respectively.

3.7 Implications for *in situ* calcite U-Pb dating

3.7.1 Selection of ICP-MS instrumentations

Early studies focused on calcite U-Pb dating using the ID-TIMS technique (Moorbath et al., 1987; Smith et al., 1991; Woodhead et al., 2006; Woodhead et al., 2012; Woodhead and Petrus, 2019; Engel et al., 2020). However, this technique requires time-intensive sample dissolution and column chemistry to produce reliable measurements. With the advent of LA-ICP-MS, sample throughput has greatly increased and the costs have been reduced substantially. All three types of ICP-MS instrumentation (i.e. Q-ICP-MS, SF-ICP-MS, and MC-ICP-MS) have been utilized for *in situ* calcite U-Pb dating (Kylander-Clark, 2020; Supplement Table S1). MC-ICP-MS provides the highest sensitivity, and by a factor of 3–5 greater than SF-ICP-MS, and >10 than Q-ICP-MS. This allows precise measurement of samples with low levels of Pb (i.e. young and/or low Pb contents). A further advantage of

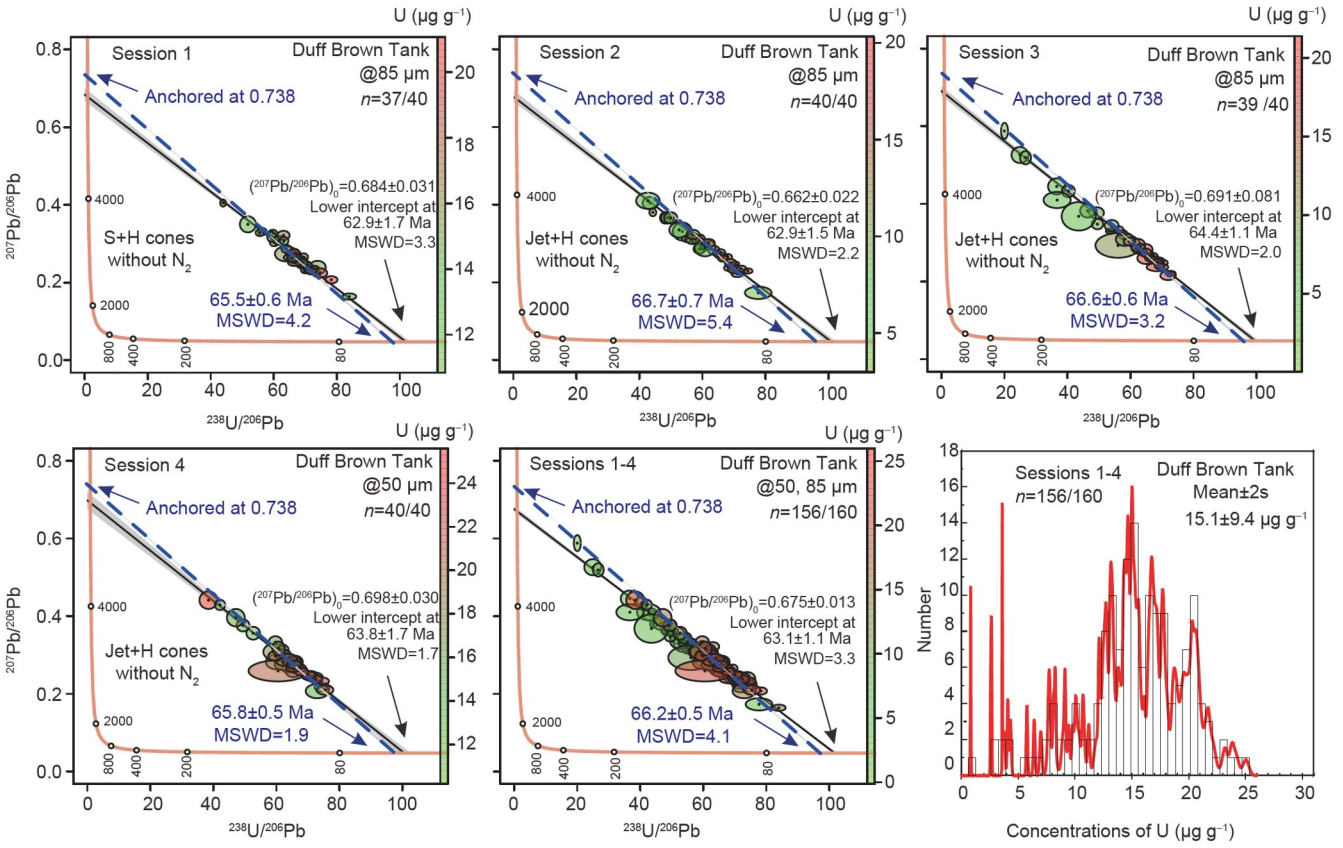

Figure 7 Tera-Wasserburg diagrams for LA-SF-ICP-MS data from the Duff Brown Tank RM. Blue dotted discordia lines are anchored at a $^{207}Pb/^{206}Pb$ ratio of 0.738 (Hill et al., 2016). Black solid lines are unconstrained discordia. The U concentrations are reflected by the relative probability. Four sessions were carried out on different days. The laser spot size used was 85 μm for sessions 1–3 and 50 μm for session 4. Session 1 was carried out using S+H cones without the addition of nitrogen, whereas sessions 2–4 were carried out using Jet+H cones without the addition of nitrogen. Several data are identified as outliers. In *n*=*a*/*b*, "*a*" indicate the numbers used for plotting and "*b*" represents the total numbers of analyses. Data were plotted and evaluated using IsoplotR (Vermeesch, 2018).

MC-ICP-MS is the simultaneous measurement of all isotopes, improving the stability of transient signals owing to the elimination of the ICP flicker. However, MC-ICP-MS instruments are expensive and require cross-calibration of the multiple ion detectors. Because of the detection capabilities of the Faraday collectors (>5 mV) and ion counters (< 2,000,000 cps), there are some limitation to the collector array arrangement that can be used to measure U and Pb in calcite.

SF-ICP-MS and Q-ICP-MS instruments measure the ion beam sequentially using a single detector, normally a secondary electron multiplier (SEM), although some instruments utilize a Faraday cup. As only one SEM is typically used, there is no need to cross-calibrate multiple detectors, which yields a simpler data reduction and analysis routine. The Faraday cup allows a greater dynamic range of measurement, but its use can add additional uncertainty to the final measurement. Another advantage of Q-ICP-MS and SF-ICP-MS is the capability to collect trace-element data in addition to U and Pb isotope data (Drost et al., 2018). However, due to the low sensitivity relative to MC-ICP-MS, a lager laser spot must be used to achieve the same measurement precision for a Q-ICP-MS and SF-ICP-MS. As indicated in Supplement Table S4, the laser spot size is generally >200 μm for Q-ICP-MS, 100–200 μm for SF-ICP-MS, and ~100 μm for MC-ICP-MS. However, our technique using the high-sensitivity combinations (Jet+X) with the addition of nitrogen permits a spot size of 50–110 μm for U-Pb dating of most calcites.

3.7.2 *Importance of the image-guided approach*

At present, there is lack of predictive criteria that can be used in the field or laboratory to screen samples prior to analysis for high U and low common Pb (as revealed by ^{204}Pb) domains (Roberts et al., 2020; Rasbury et al., 2021). Incorporation of U into calcite is not well understood in many environments. This is because trace element incorporation in calcite is not only dominated by thermodynamics, but also by a large number of phenomenological factors including trace-element availability, calcite growth rate, temperature, pH, Eh, pCO_2, the Ca^{2+}: CO_3^{2-} ratio in solution, ionic radius, and U complexation (Roberts et al., 2020). A range of non-destructive imaging techniques have been used for sample screening, including optical microscopy, cathodoluminescence (CL), charge contrast imaging,

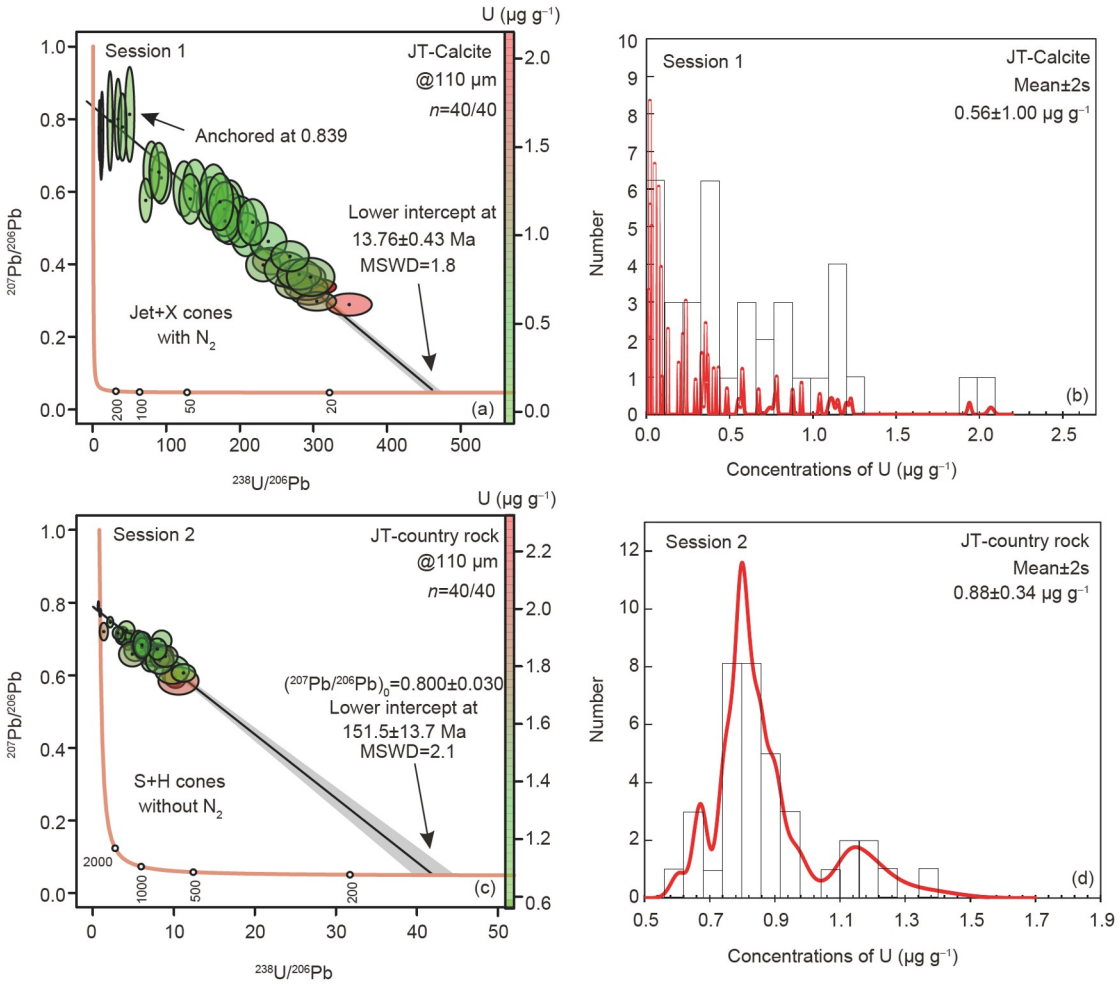

Figure 8 Tera-Wasserburg diagrams for LA-SF-ICP-MS data for sample JT showing intercept ages. Concentrations of U are reflected by the relative probability. (a) & (b) Session 1 for the calcite veins (the left and paler part of Figure 6 (JT) was carried out using Jet+X cones with the addition of nitrogen. The discordia lines in the Tera-Wasserburg diagrams are anchored to a $^{207}Pb/^{206}Pb$ ratio of 0.839 (Guillong et al., 2020). (c) & (d) Session 2 for the country rock (the right and darker part of Figure 6 (JT)) was carried out using S+H cones without the addition of nitrogen. The lower intercept age was calculated using unconstrained discordia. The laser spot size used was 110 μm. Several data are identified as outliers. In $n = a/b$, "a" indicates the numbers used for plotting and "b" represents the total number of analyses. Data were plotted and evaluated using IsoplotR (Vermeesch, 2018).

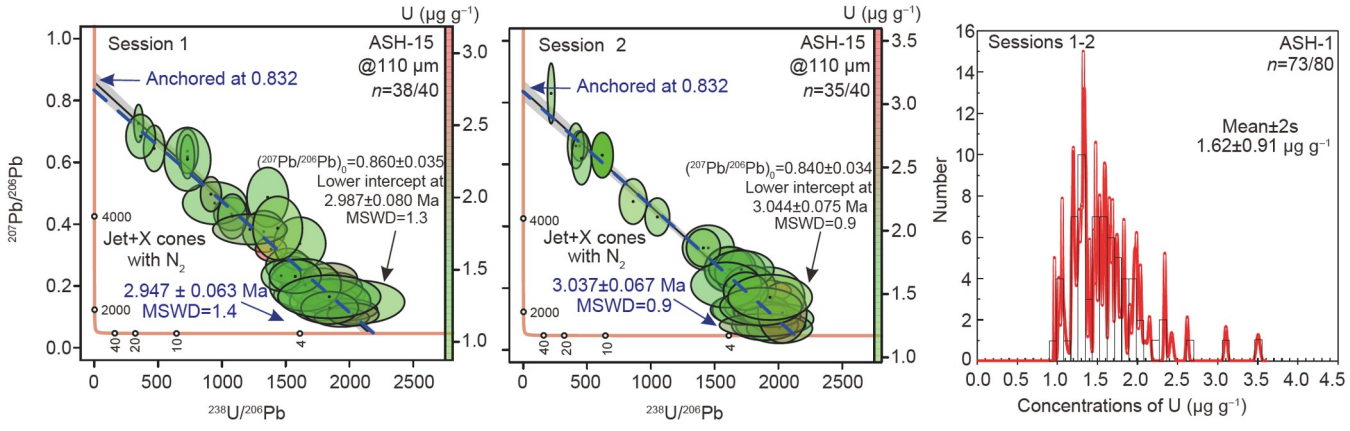

Figure 9 Intercept ages and U contents for ASH-1; intercept ages are shown in Tera-Wasserburg plots. Blue dotted discordia lines in the Tera-Wasserburg diagrams are anchored to a $^{207}Pb/^{206}Pb$ ratio of 0.832 (Nuriel et al., 2021). Black solid lines are unconstrained discordia. The U concentrations are reflected by the relative probability. Two sessions were carried out on different days. Sessions 1 and 2 were carried out using Jet+X cones with the addition of nitrogen and a spot size of 110 μm. Several data are identified as outliers. In $n = a/b$, "a" indicates the numbers used for plotting and "b" represents the total number of analyses. Data were plotted and evaluated using IsoplotR (Vermeesch, 2018).

back-scattered electron imaging (BSE), and synchtron X-ray florescence (XRF) mapping (Roberts et al., 2020; Rasbury et al., 2021). Traditionally, these techniques were used to identify and characterize calcite growth stages or alterations, but not for the identification of high U and low common-Pb domains.

Previous studies have applied spot or line scanning traverses to screen out the high U and low common Pb domains suitable for U-Pb dating, either by monitoring the ^{204}Pb and ^{238}U signal intensity, and making a note of suitable locations, then a second-step of U-Pb dating is carried out on these domains ("spot traverse" approach). Alternatively, LA-ICP-MS mapping technique was used to determine both the location and nature of U and Pb zonation in unknown samples ("imaging-guided dating" approach; Roberts et al., 2020, 2021). Spot traverses provide rapid screening of multiple samples or aliquots, whereas mapping provides more detail across complex heterogeneous samples. In this study, we compared these two strategies for an unknown sample. Figure 10a–10b shows the data plotted using the spot tra-

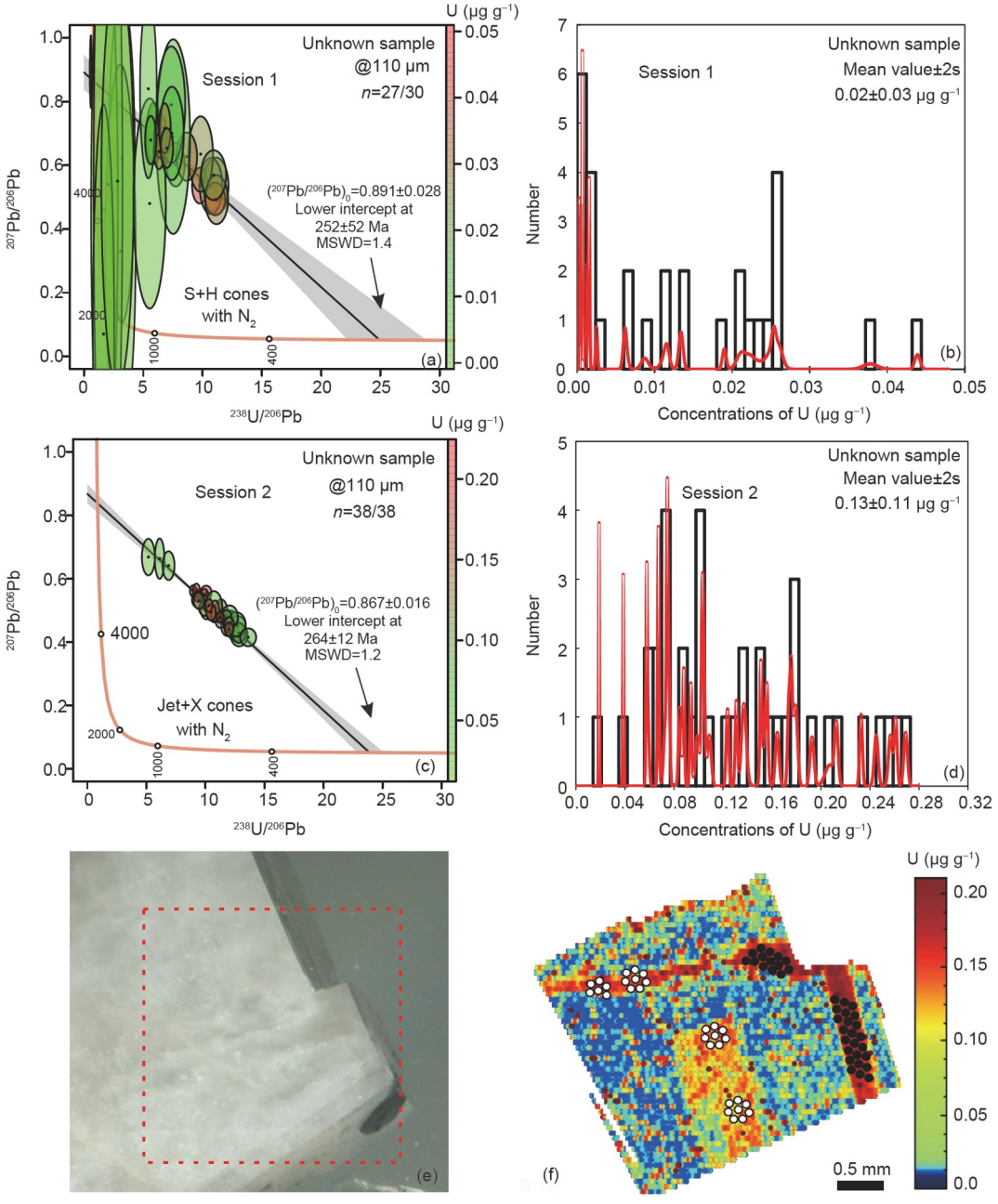

Figure 10 Plots comparing age data from an unknown sample using spot-traverses and imaging-guided dating strategies. Session 1 was carried out using S+H cones with the addition of nitrogen, whereas Session 2 used Jet+X cones with the addition of nitrogen. No data were identified as outliers. Corresponding images in optical light are provided as (e). Empty circles and Filled circles in (f) represent the locations analyzed using spot-traverses (Session 1) and the locations analyzed using imaging-guided dating strategies (Session 2), respectively. Data were plotted and evaluated using IsoplotR (Vermeesch, 2018).

verse approach, whereas Figure 10c–10d shows the results obtained using "image-guided dating" (see also Supplement Table S5). Clearly, the image-guided dating approach provides better results because of the more accurately targeting the high U domains. Based on our laser parameters, imaging of a 5 mm×5 mm area requires <60 mins, but provides a useable level of spatial resolution.

3.7.3 Development of new calcite U-Pb reference materials

Accurate LA-ICP-MS calcite U-Pb dating requires matrix-matched RMs for the correction of instrumental mass bias of Pb/U ratios. Several in-house materials are currently being used as RMs, including Duff Brown Tank, ASH-15, JT, and AHX-1A. Sample WC-1 (ID-TIMS age of 254.4±6.5 Ma; Roberts et al., 2020) is the only well-characterized RM that is distributed across most laboratories that date calcite. Sample ASH-15 has also been characterized by ID-TIMS (Nuriel et al., 2021) and has been shared with a growing number of laboratories. The relatively high uncertainty (2.5%) on the age of WC-1 sets a minimum uncertainty on any unknown age determination. In addition, compositional heterogeneity in WC-1 has been reported (Guillong et al., 2020), such that some samples of WC-1 may have larger Pb/U isotopic variability than described by Roberts et al. (2017). Supplement Table S6 summarizes the commonly used calcite U-Pb RMs, along with some additional materials characterized for method development. Most of these RMs are not well characterized using ID-TIMS technique, but are used as in-house RMs.

The development of matrix-matched RMs remains a major hurdle to accurate and precise LA analysis of carbonate minerals because of the variable mineralogy (calcite, dolomite, and aragonite) texture, composition (e.g., high-magnesium calcite), and ages (e.g., >500 Ma). Textural differences (e.g., microcrystalline) between the unknown and RMs can contribute to high uncertainties due to differences in ablation efficiency, LIEF, and crater morphology (Elisha et al., 2021). Observed deviations are potentially up to 20% of the final intercept age depending on crater geometry and/or matrix effects (Guillong et al., 2020). The currently available RMs are unable to meet the requirements, in particular for dolomite and aragonite.

4. Conclusions

U-Pb geochronology of calcite by laser ablation inductively coupled plasma mass spectrometry (LA-ICP-MS) is an emerging field with potential to solve a vast array of geological problems. Owing to low contents of U and Pb, measurement by more sensitive instruments, such as sector field (SF)-ICP-MS is advantageous. We show that a Jet+X cone combination with the addition of nitrogen provides the best sensitivity for measuring U-Pb isotopes using a Thermo Element XR. This setup improves the precision on calcite U-Pb data for samples with low U and radiogenic Pb, and increases the spatial resolution below 100 μm. LIEFs of $^{206}Pb/^{238}U$ ratios when using shallow crater geometries in NIST SRM 614, ARM-3 and WC-1 RMs are insignificant (<2.2%). Adopting the optimized instrument parameters, results from three commonly used calcite U-Pb reference materials (Duff Brown Tank, JT, and ASH-15) match well with the published ID-TIMS data, demonstrating the reliability of our technique. In addition, we demonstrate that ARM-3 is an appropriate RM for $^{207}Pb/^{206}Pb$ calibration and instrument tuning. The image-guided approach is shown to be an efficient method for obtaining robust ages.

Acknowledgements *Perach NURIEL, Victor POLYAK and Marcel GUILLONG are acknowledged for providing the ASH-15, Duff Brown Tank, and JT RMs, respectively. Hongxia MA is thanked for sample preparation. Liangliang ZHANG is thanked for the providing of LA-MC-ICP-MS data. This work was co-supported by the National Key R&D Program of China (Grant No. 2018YFA0702602), the National Natural Science Foundation of China (Grant Nos. 41903024, 41525012), and the Youth Innovation Promotion Association of the Chinese Academy of Sciences (Grant No. 2022066).*

References

Bouman C, Deerberg M, Schwieters J. 2009. NEPTUNE and NEPTUNE Plus: Breakthrough in Sensitivity using a Large Interface Pump and New Sample Cone. Thermo Fischer Scientific Application Note: 30187, https://www.analyteguru.com/t5/Scientific-Library/NEPTUNE-and-NEPTUNE-Plus-Breakthrough-in-Sensitivity-using-a/ta-p/4994

Burisch M, Gerdes A, Walter B F, Neumann U, Fettel M, Markl G. 2017. Methane and the origin of five-element veins: mineralogy, age, fluid inclusion chemistry and ore forming processes in the Odenwald, SW Germany. Ore Geol Rev, 81: 42–61

Cheng T, Zhao J, Feng Y, Pan W, Liu D. 2020. *In-situ* LA-MC-ICPMS U-Pb dating method for low-uranium carbonate minerals. Chin Sci Bull, 65: 150–154

Coogan L A, Parrish R R, Roberts N M W. 2016. Early hydrothermal carbon uptake by the upper oceanic crust: Insight from *in situ* U-Pb dating. Geology, 44: 147–150

Drost K, Chew D, Petrus J A, Scholze F, Woodhead J D, Schneider J W, Harper D A T. 2018. An image mapping approach to U-Pb LA-ICP-MS carbonate dating and applications to direct dating of carbonate sedimentation. Geochem Geophys Geosyst, 19: 4631–4648

Elisha B, Nuriel P, Kylander-Clark A, Weinberger R. 2021. Towards in situ U-Pb dating of dolomite. Geochronology, 3: 337–349

Engel J, Maas R, Woodhead J, Tympel J, Greig A. 2020. A single-column extraction chemistry for isotope dilution U-Pb dating of carbonate. Chem Geol, 531: 119311

Goodfellow B W, Viola G, Bingen B, Nuriel P, Kylander-Clark A R C. 2017. Palaeocene faulting in SE Sweden from U-Pb dating of slickenfibre calcite. Terra Nova, 29: 321–328

Guillong M, Wotzlaw J F, Looser N, Laurent O. 2020. Evaluating the reliability of U-Pb laser ablation inductively coupled plasma mass spectrometry (LA-ICP-MS) carbonate geochronology: Matrix issues and a potential calcite validation reference material. Geochronology, 2: 155–167

Hansman R J, Albert R, Gerdes A, Ring U. 2018. Absolute ages of multiple generations of brittle structures by U-Pb dating of calcite. Geology, 46:

207–210
He T, Ni Q, Miao Q, Li M. 2018. Effects of cone combinations on the signal enhancement by nitrogen in LA-ICP-MS. J Anal At Spectrom, 33: 1021–1030
Hill C A, Polyak V J, Asmerom Y, P. Provencio P. 2016. Constraints on a Late Cretaceous uplift, denudation, and incision of the Grand Canyon region, southwestern Colorado Plateau, USA, from U-Pb dating of lacustrine limestone. Tectonics, 35: 896–906
Hoareau G, Claverie F, Pecheyran C, Paroissin C, Grignard P A, Motte G, Chailan O, Girard J P. 2021. Direct U-Pb dating of carbonates from micron-scale femtosecond laser ablation inductively coupled plasma mass spectrometry images using robust regression. Geochronology, 3: 67–87
Holdsworth R E, McCaffrey K J W, Dempsey E, Roberts N M W, Hardman K, Morton A, Feely M, Hunt J, Conway A, Robertson A. 2019. Natural fracture propping and earthquake-induced oil migration in fractured basement reservoirs. Geology, 47: 700–704
Hu Z, Liu Y, Gao S, Liu W, Zhang W, Tong X, Lin L, Zong K, Li M, Chen H, Zhou L, Yang L. 2012. Improved *in situ* Hf isotope ratio analysis of zircon using newly designed X skimmer cone and jet sample cone in combination with the addition of nitrogen by laser ablation multiple collector ICP-MS. J Anal At Spectrom, 27: 1391–1399
Hu Z, Gao S, Liu Y, Hu S, Chen H, Yuan H. 2008. Signal enhancement in laser ablation ICP-MS by addition of nitrogen in the central channel gas. J Anal At Spectrom, 23: 1093–1101
Jahn B, Cuvellier H. 1994. Pb-Pb and U-Pb geochronology of carbonate rocks: An assessment. Chem Geol, 115: 125–151
Jeffries T E, Fernandez-Suarez J, Corfu F, Gutierrez Alonso G. 2003. Advances in U-Pb geochronology using a frequency quintupled Nd:YAG based laser ablation system (λ=213 nm) and quadrupole based ICP-MS. J Anal At Spectrom, 18: 847–855
Jeffries T E, Jackson S E, Longerich H P. 1998. Application of a frequency quintupled Nd:YAG source (λ=213 nm) for laser ablation inductively coupled plasma mass spectrometric analysis of minerals. J Anal At Spectrom, 13: 935–940
Jochum K P, Weis U, Stoll B, Kuzmin D, Yang Q, Raczek I, Jacob D E, Stracke A, Birbaum K, Frick D A, Günther D, Enzweiler J. 2011. Determination of reference values for NIST SRM 610-617 glasses following ISO guidelines. Geostand Geoanal Res, 35: 397–429
Kurumada Y, Aoki S, Aoki K, Kato D, Saneyoshi M, Tsogtbaatar K, Windley B F, Ishigaki S. 2020. Calcite U-Pb age of the Cretaceous vertebrate-bearing Bayn Shire Formation in the Eastern Gobi Desert of Mongolia: Usefulness of caliche for age determination. Terra Nova, 32: 246–252
Kylander-Clark A R C. 2020. Expanding the limits of laser-ablation U-Pb calcite geochronology. Geochronology, 2: 343–354
Li Q, Parrish R R, Horstwood M S A, McArthur J M. 2014. U-Pb dating of cements in Mesozoic ammonites. Chem Geol, 376: 76–83
Luo K, Zhou J X, Feng Y X, Uysal I T, Nguyen A, Zhao J X, Zhang J. 2020. *In situ* U-Pb dating of calcite from the South China antimony metallogenic belt. iScience, 23: 101575
Montano D, Gasparrini M, Gerdes A, Della Porta G, Albert R. 2021. *In-situ* U-Pb dating of Ries Crater lacustrine carbonates (Miocene, South-West Germany): Implications for continental carbonate chronostratigraphy. Earth Planet Sci Lett, 568: 117011
Moorbath S, Taylor P N, Orpen J L, Treloar P, Wilson J F. 1987. First direct radiometric dating of Archaean stromatolitic limestone. Nature, 326: 865–867
Nuriel P, Craddock J, Kylander-Clark A R C, Uysal I T, Karabacak V, Dirik R K, Hacker B R, Weinberger R. 2019. Reactivation history of the North Anatolian fault zone based on calcite age-strain analyses. Geology, 47: 465–469
Nuriel P, Weinberger R, Kylander-Clark A R C, Hacker B R, Craddock J P. 2017. The onset of the Dead Sea transform based on calcite age-strain analyses. Geology, 45: 587–590
Nuriel P, Wotzlaw J F, Ovtcharova M, Vaks A, Stremtan C, Šala M, Roberts N M W, Kylander-Clark A R C. 2021. The use of ASH-15 flowstone as a matrix-matched reference material for laser-ablation U-Pb geochronology of calcite. Geochronology, 3: 35–47
Pagel M, Bonifacie M, Schneider D A, Gautheron C, Brigaud B, Calmels D, Cros A, Saint-Bezar B, Landrein P, Sutcliffe C, Davis D, Chaduteau C. 2018. Improving paleohydrological and diagenetic reconstructions in calcite veins and breccia of a sedimentary basin by combining Δ47 temperature, δ^{18}O water and U-Pb age. Chem Geol, 481: 1–17
Pan L, Shen A, Zhao J, Hu A, Hao Y, Liang F, Feng Y, Wang X, Jiang L. 2020. LA-ICP-MS U-Pb geochronology and clumped isotope constraints on the formation and evolution of an ancient dolomite reservoir: The Middle Permian of northwest Sichuan Basin (SW China). Sediment Geol, 407: 105728
Parrish R R, Parrish C M, Lasalle S. 2018. Vein calcite dating reveals Pyrenean orogen as cause of Paleogene deformation in southern England. J Geol Soc, 175: 425–442
Paton C, Hellstrom J, Paul B, Woodhead J, Hergt J. 2011. Iolite: Freeware for the visualisation and processing of mass spectrometric data. J Anal At Spectrom, 26: 2508–2518
Paton C, Woodhead J D, Hellstrom J C, Hergt J M, Greig A, Maas R. 2010. Improved laser ablation U-Pb zircon geochronology through robust downhole fractionation correction. Geochem Geophys Geosyst, 11: Q0AA06
Paul B, Paton C, Norris A, Woodhead J, Hellstrom J, Hergt J, Greig A. 2012. CellSpace: A module for creating spatially registered laser ablation images within the Iolite freeware environment. J Anal At Spectrom, 27: 700–706
Petrus J A, Chew D M, Leybourne M I, Kamber B S. 2017. A new approach to laser-ablation inductively-coupled-plasma mass-spectrometry (LA-ICP-MS) using the flexible map interrogation tool 'Monocle'. Chem Geol, 463: 76–93
Petrus J A, Kamber B S. 2012. VizualAge: A novel approach to laser ablation ICP-MS U-Pb geochronology data reduction. Geostand Geoanal Res, 36: 247–270
Rasbury E T, Present T M, Northrup P, Tappero R V, Lanzirotti A, Cole J M, Wooton K M, Hatton K. 2021. Tools for uranium characterization in carbonate samples: case studies of natural U-Pb geochronology reference materials. Geochronology, 3: 103–122
Ring U, Gerdes A. 2016. Kinematics of the Alpenrhein-Bodensee graben system in the Central Alps: Oligocene/Miocene transtension due to formation of the Western Alps arc. Tectonics, 35: 1367–1391
Roberts N M W, Drost K, Horstwood M S A, Condon D J, Chew D, Drake H, Milodowski A E, McLean N M, Smye A J, Walker R J, Haslam R, Hodson K, Imber J, Beaudoin N, Lee J K. 2020. Laser ablation inductively coupled plasma mass spectrometry (LA-ICP-MS) U-Pb carbonate geochronology: Strategies, progress, and limitations. Geochronology, 2: 33–61
Roberts N M W, Rasbury E T, Parrish R R, Smith C J, Horstwood M S A, Condon D J. 2017. A calcite reference material for LA-ICP-MS U-Pb geochronology. Geochem Geophys Geosyst, 18: 2807–2814
Roberts N M W, Walker R J. 2016. U-Pb geochronology of calcite-mineralized faults: Absolute timing of rift-related fault events on the northeast Atlantic margin. Geology, 44: 531–534
Roberts N M W, Žák J, Vacek F, Sláma J. 2021. No more blind dates with calcite: Fluid-flow vs. fault-slip along the Očkov thrust, Prague Basin. Geosci Front, 12: 101143
Rochelle-Bates N, Roberts N M W, Sharp I, Freitag U, Verwer K, Halton A, Fiordalisi E, van Dongen B E, Swart R, Ferreira C H, Dixon R, Schröder S. 2021. Geochronology of volcanically associated hydrocarbon charge in the pre-salt carbonates of the Namibe Basin, Angola. Geology, 49: 335–340
Schaltegger U, Schmitt A K, Horstwood M S A. 2015. U-Th-Pb zircon geochronology by ID-TIMS, SIMS, and laser ablation ICP-MS: Recipes, interpretations, and opportunities. Chem Geol, 402: 89–110
Shen A, Hu A, Cheng T, Liang F, Pan W, Feng Y, Zhao J. 2019. Laser ablation *in situ* U-Pb dating and its application to diagenesis-porosity evolution of carbonate reservoirs. Pet Explor Dev, 46: 1127–1140
Smith P E, Farquhar R M, Hancock R G. 1991. Direct radiometric age

determination of carbonate diagenesis using U-Pb in secondary calcite. Earth Planet Sci Lett, 105: 474–491
Vermeesch P. 2018. IsoplotR: A free and open toolbox for geochronology. Geosci Front, 9: 1479–1493
Woodhead J, Hellstrom J, Maas R, Drysdale R, Zanchetta G, Devine P, Taylor E. 2006. U–Pb geochronology of speleothems by MC-ICPMS. Quat Geochronol, 1: 208–221
Woodhead J, Hellstrom J, Pickering R, Drysdale R, Paul B, Bajo P. 2012. U and Pb variability in older speleothems and strategies for their chronology. Quat Geochronol, 14: 105–113
Woodhead J, Petrus J. 2019. Exploring the advantages and limitations of *in situ* U-Pb carbonate geochronology using speleothems. Geochronology, 1: 69–84
Wu C C, Burger M, Günther D, Shen C C, Hattendorf B. 2018. Highly-sensitive open-cell LA-ICPMS approaches for the quantification of rare earth elements in natural carbonates at parts-per-billion levels. Anal Chim Acta, 1018: 54–61
Wu S, Xu C, Simon K, Xiao Y, Wang Y. 2017. Study on Ablation behaviors and Ablation Rates of a 193 nm ArF Excimer Laser System for Selected Substrates in LA-ICP-MS Analaysis (in Chinese with English Abstract). Rock Miner Anal, 36: 451–459
Wu S, Wörner G, Jochum K P, Stoll B, Simon K, Kronz A. 2019. The preparation and preliminary characterisation of three synthetic andesite reference glass materials (ARM-1, ARM-2, ARM-3) for *in Situ* Microanalysis. Geostand Geoanal Res, 43: 567–584
Wu S, Yang M, Yang Y, Xie L, Huang C, Wang H, Yang J. 2020a. Improved *in situ* zircon U-Pb dating at high spatial resolution (5–16 μm) by laser ablation-single collector-sector field-ICP-MS using Jet sample and X skimmer cones. Int J Mass Spectrom, 456: 116394
Wu S, Yang Y, Wang H, Huang C, Xie L, Yang J. 2020b. Characteristic performance of guard electrode in LA-SF-ICP-MS for multi-element quantification. Atom Spectro, 41: 154–161
Wu S, Yang Y, Jochum K P, Romer R L, Glodny J, Savov I P, Agostini S, De Hoog J C M, Peters S T M, Kronz A, Zhang C, Bao Z, Wang X, Li Y, Tang G, Feng L, Yu H, Li Z, Zhang L, Lin J, Zeng Y, Xu C, Wang Y, Cui Z, Deng L, Xiao J, Liu Y, Xue D, Zhang D, Jia L, Wang H, Xu L, Huang C, Xie L, Pack A, Wörner G, He M, Li C, Yuan H, Huang F, Li Q, Yang J, Li X, Wu F. 2021. Isotopic Compositions (Li-B-Si-O-Mg-Sr-Nd-Hf-Pb) and $Fe^{2+}/\Sigma Fe$ Ratios of Three Synthetic Andesite Glass Reference Materials (ARM-1, ARM-2, ARM-3). Geostand Geoanal Res, 45: 719–745
Yang M, Yang Y H, Wu S T, Romer R L, Che X D, Zhao Z F, Li W S, Yang J H, Wu F Y, Xie L W, Huang C, Zhang D, Zhang Y. 2020. Accurate and precise *in situ* U-Pb isotope dating of wolframite series minerals *via* LA-SF-ICP-MS. J Anal At Spectrom, 35: 2191–2203
Yang P, Wu G, Nuriel P, Nguyen A D, Chen Y, Yang S, Feng Y, Ren Z, Zhao J. 2021. *In situ* LA-ICPMS U-Pb dating and geochemical characterization of fault-zone calcite in the central Tarim Basin, northwest China: Implications for fluid circulation and fault reactivation. Chem Geol, 568: 120125
Yang Y, Yang M, Wang H, Yang J, Wu F. 2021. Methodology for *in situ* wolframite U-Pb dating and its application. Sci China Earth Sci, 64: 187–190
Yokoyama T, Kimura J, Mitsuguchi T, Danhara T, Hirata T, Sakata S, Iwano H, Maruyama S, Chang Q, Miyazaki T, Murakami H, Saito-Kokubu Y. 2018. U-Pb dating of calcite using LA-ICP-MS: Instrumental setup for non-matrix-matched age dating and determination of analytical areas using elemental imaging. Geochem J, 52: 531–540
Zhang L, Zhu D, Yang Y, Wang Q, Xie J, Zhao Z. 2021. U-Pb geochronology of carbonate by Laser Ablation MC-ICPMS: Method improvements and geological applications. At Spectrom, 42: 335–348

(Responsible editor: Yongsheng LIU)